CHEMISTRY
A EUROPEAN JOURNAL

DOI: 10.1002/chem.200901479

On the Electronic Structure of Ni^{II} Complexes That Feature Chelating Bisguanidine Ligands

Pascal Roquette,[a] Astrid Maronna,[a] Anastasia Peters,[a] Elisabeth Kaifer,[a] Hans-Jörg Himmel,*[a] Christoph Hauf,[b] Verena Herz,[b] Ernst-Wilhelm Scheidt,[b] and Wolfgang Scherer*[b]

Dedicated to Professor Hubert Schmidbaur on the occasion of his 75th birthday

Abstract: In this work we report on the syntheses and properties of several new Ni complexes featuring the chelating bisguanidines bis(tetramethylguanidino)benzene (btmgb), bis(tetramethylguanidino)naphthalene (btmgn), and bis(tetramethylguanidino)biphenyl (btmgbp) as ligands. All complexes were structurally characterized by single-crystal X-ray diffraction and quantum chemical calculations. A detailed inspection of the magnetic susceptibility of [(btmgb)NiX_2] and [(btmgbp)NiX_2] (X = Cl, Br) revealed a linear temperature dependence of $\chi^{-1}(T)$ above 50 K, which was in agreement with a Curie–Weiss-type behavior and a triplet ground state. Below approximately 25 K, however, magnetic susceptibility studies of the paramagnetic d^8 Ni complexes revealed the presence of a significant zero-field splitting (ZFS) that results from spin–orbit mixing of excited states into the triplet ground state. The electronic consequences that might arise from the mixing of states as well as from a possible non-innocent behavior of the ligand have been explored by an experimental charge density study of [(btmgb)$NiCl_2$] at low temperatures (7 K). Here, the presence of ZFS was identified as one potential reason for the flat ∢Cl-Ni-Cl deformation potential and the distinct differences between the ∢X-Ni-X valence angles observed by experiment and predicted by DFT. An analysis of the topology of the experimentally and theoretically derived electron-density distributions of [(btmgb)$NiCl_2$] confirmed the strong donor character of the bisguanidine ligand but clearly ruled out any significant non-innocent ligand (NIL) behavior. Hence, [(btmgb)$NiCl_2$] provides an experimental reference system to study the mixing of certain excited states into the ground state unbiased from any competing NIL behavior.

Keywords: chelates · coordination compounds · electron density · guanidines · nickel

Introduction

The interest in guanidines as a useful class of ligands derives from their diversified coordination chemistry as either neutral or charged systems and furthermore from their ability to act as superior σ-electron donors.[1] With relevance to this work, Sundermeyer et al. reported on the new superbasic proton sponge 1,8-bis(tetramethylguanidino)naphthalene (btmgn) as an example for an aromatically bridged bisguanidine.[2] In general, by bridging two or more guanidine units a library of ligands for a large variety of tasks and requirements is accessible. For example, in the field of biomimetic coordination chemistry, peralkylated bifunctional nitrogen ligands for Cu and Fe were designed,[3,4] and in the transfer hydrogenation of acetophenone, Mo and Ru complexes of these ligands demonstrated their catalytic potential.[5]

[a] Dipl.-Chem. P. Roquette, Dipl.-Chem. A. Maronna, Dipl.-Chem. A. Peters, Dr. E. Kaifer, Prof. Dr. Dr. H.-J. Himmel
Anorganisch-Chemisches Institut
Ruprecht-Karls-Universität Heidelberg
Im Neuenheimer Feld 270, 69120 Heidelberg (Germany)
Fax: (+49) 6221-545707
E-mail: hans-jorg.himmel@aci.uni-heidelberg.de

[b] Dipl.-Phys. C. Hauf, Dipl.-Phys. V. Herz, Dr. E.-W. Scheidt, Prof. Dr. W. Scherer
Institut für Physik, Universität Augsburg
86135 Augsburg (Germany)
Fax: (+49) 821-5983227
E-mail: wolfgang.scherer@physik.uni-augsburg.de

Supporting information for this article is available on the WWW under http://dx.doi.org/10.1002/chem.200901479. It includes cyclic voltammetric studies of btmgb; details of the crystal-structure analyses; the combined experimental and theoretical charge-density study of [(btmgb)$NiCl_2$]; experimental and theoretical ∢X-Ni-X valence angles; the Kohn–Sham spin orbitals of [(btmgb)$NiCl_2$]; and details of the magnetic susceptibility studies.

WILEY InterScience DISCOVER SOMETHING GREAT

© 2010 Wiley-VCH Verlag GmbH & Co. KGaA, Weinheim

Brookhart et al. discovered the ability of diimine ligands coordinated to late-transition metals, especially Ni, Pd, and Pt, to catalyze polymerization of ethylene and other α-olefin molecules.[6] These findings stimulated an interest in the detailed understanding of the electronic structure of such systems. Nickel–bis(diimine) complexes in particular received growing attention, among others by Wieghardt et al., who shaped the concept of non-innocent ligands.[7] Combined experimental and theoretical investigations on such systems showed that the ligand plays a significant role in the electron transfer inside the complex.[8,9] In particular, the analysis of the different electronic states and their frontier orbitals and spin-density distributions provided valuable insight into the properties of non-innocent diimine ligands.

Aromates functionalized with several guanidino groups are potentially strong electron donors. Hence, some of us recently showed that tetrakis(tetramethylguanidino)benzene (ttmgb; see Scheme 1) can be oxidized readily, for example,

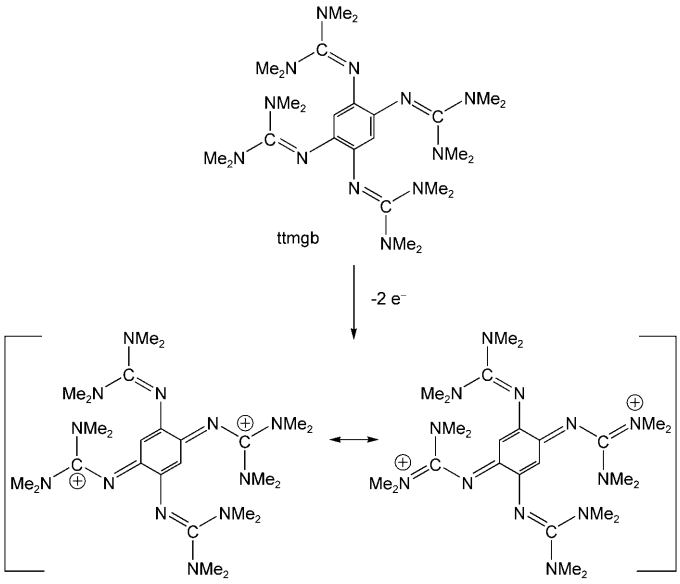

Scheme 1. Tetrakis(tetramethylguanidino)benzene (ttmgb) can be readily oxidized in air or by I_2. In its oxidized form, the positive charges are delocalized as shown here by the resonance structures.

by O_2 in the air or by I_2.[10] A two-electron oxidation wave was measured at $E_{1/2}(CH_3CN) = -0.32$ V versus SCE (see Figure S1 in the Supporting Information). In its oxidized form, the positive charges are delocalized, with two of the resonance structures being sketched in Scheme 1. In principle, ttmgb can be classified as a potentially non-innocent ligand (NIL)[11,12] that does not necessarily display a closed-shell configuration. Thus, ligand-centered redox reactions might play a role in the case of the ttmgb ligand. One of the prime examples of an NIL system is the dianion of *ortho*-phenylenediamine (opda) and its derivatives.[13,14] Both the btmgb and the opda ligand display a bridging phenylene unit that can participate in π-electron delocalization. Accordingly, the Lewis formula of metal complexes of these

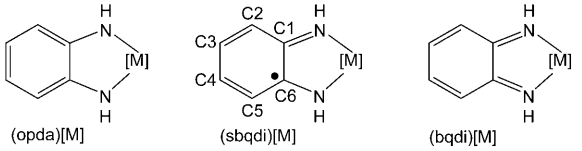

species can be formulated in different ways. The most likely electronic structure can be estimated on the basis of structural data by inspection of the C–C bond lengths within the benzene ring and also of the C–N bond lengths. For example, the C2–C3 and C4–C5 bond lengths in the Co^{II} complex $[Co(sbqdi)_2]$ (sbqdi = semi-*o*-benzoquinonediimine) are significantly shorter than the other phenylene ring C–C bond lengths.[15] In addition, the C–N bond lengths are relatively short (1.348–1.371(8) Å). Another more recent example is provided by the complex $[Ni(^{F}sbqdi)_2]$ (^{F}sbqdi denotes an sbqdi ligand in which both hydrogen atoms bound to nitrogen are substituted by pentafluorophenyl groups).[16] Again, two of the C–C bond lengths (C2–C3 and C4–C5) within each of the C_6 rings were found to be relatively short (1.350(6) and 1.352(7) Å), whereas the others cover the range 1.409(6)–1.429(6) Å. A more pronounced benzoquinonediimine-type electron distribution is found in case of $[Ru(bqdi)(PPh_3)_2(MeCN)_2](PF_6)_2$:[17] 1.354(5) Å for C2–C3 and C4–C5 and 1.435(4)–1.457(5) Å for the remaining C–C bond lengths in the C_6 moiety.

In this work we examine d^8 Ni complexes of the three bisguanidines btmgb,[18] btmgn,[2] and btmgbp[19], which exhibit

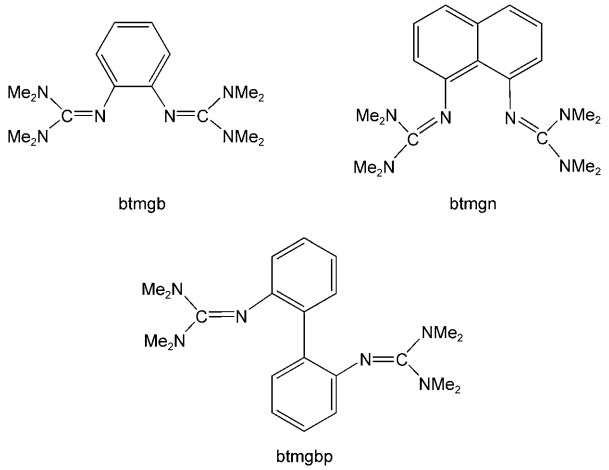

a weaker reduction potential than ttmgb (see Figure S1 in the Supporting Information). All of these complexes represent examples of tetrahedrally coordinated Ni complexes in an open-shell configuration. The chelating ligand btmgbp offers a relatively large flexibility due to a low barrier of rotation around the central C–C bond. In comparison with the btmgbp ligand, the chelating btmgb and btmgn are more rigid. Recently the syntheses of Pt complexes of btmgb[20] and Pd and Pt complexes featuring the btmgn[21] ligand were

 © 2010 Wiley-VCH Verlag GmbH & Co. KGaA, Weinheim

reported. The results gathered in these previous studies will be compared with the ones attained herein.

The experimentally obtained topology of the electron-density distribution of the open-shell d^8 [(btmgb)$NiCl_2$] complex has been determined to analyze the potential non-innocent character of the ligand and its influence on the electronic structure of the complex. The effect of zero-field splitting is analyzed by magnetic measurements and its influence on the electron-density distribution is discussed. Extensive quantum chemical calculations shed further light on the electronic structure of these benchmark systems.

Results and Discussion

This section is divided into four parts. In the first one the syntheses and the structures of the complexes will be discussed, followed by a section dealing with paramagnetic NMR spectra recorded at room temperature for two of the complexes. Subsequently, the magnetic properties as derived from magnetic susceptibility measurements will be presented, and we will also report on the results of quantum chemical calculations on the lowest energy triplet and singlet electronic states of the complexes. Finally, the experimentally and theoretically determined topology of the electron-density distribution will be assessed in detail for the [(btmgb)$NiCl_2$] complex.

Syntheses and structural characterization: All Ni–bisguanidine complexes [(btmgb)NiX_2], [(btmgn)NiX_2], and [(btmgbp)NiX_2] (X = Br, Cl) can be prepared according to Equation (1) by reaction of [(dme)NiX_2] (dme = 1,2-dimethoxyethane) with the corresponding bisguanidine. Traces of water have to be rigorously excluded to avoid protonation of the ligand (the btmgn ligand is a "proton sponge"). Although all possible precautions were taken, minor quantities of protonated ligand were observed in some of the raw products. These impurities generally led to slightly higher C and N contents in the elemental analysis (see the Experimental Section). The pure compound was obtained by crystallization.

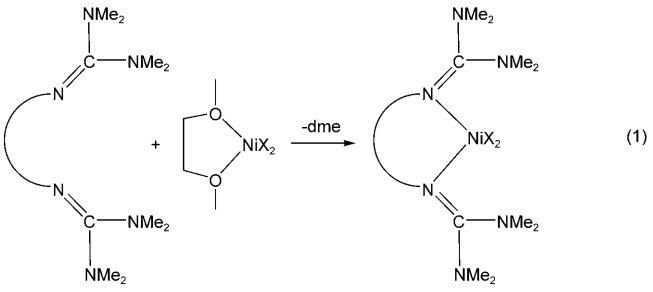

[(btmgb)NiX_2]: Figure 1 displays the molecular structure of [(btmgb)$NiCl_2$] as obtained by X-ray diffraction at 200 K. Table 1 contains selected parameters of [(btmgb)$NiCl_2$].

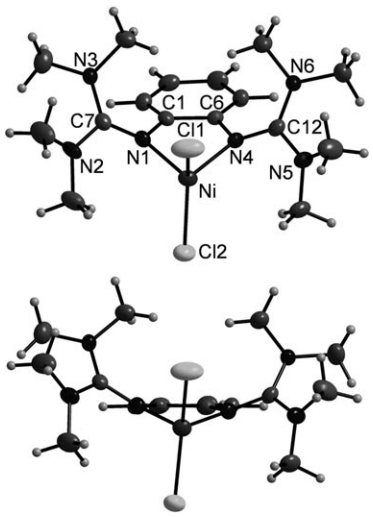

Figure 1. Molecular structure of [(btmgb)$NiCl_2$]. Ellipsoids are drawn at the 50 % probability level.

Table 1. Selected parameters (bond lengths [Å] and angles [°]) as determined by X-ray diffraction for [(btmgb)$NiCl_2$] at 200 K.

Ni–N1	2.000(4)	Ni–N4	1.993(3)
Ni–Cl1	2.2547(15)	Ni–Cl2	2.2436(13)
N1–C1	1.423(5)	N4–C6	1.408(5)
N1–C7	1.310(5)	N4–C12	1.327(5)
C7–N2	1.365(5)	C12–N5	1.353(5)
C7–N3	1.358(5)	C12–N6	1.362(5)
N1-Ni-N4	83.36(13)	Cl1-Ni-Cl2	130.66(5)
C1-N1-Ni	109.4(3)	C6-N4-Ni	110.5(2)
N1-Ni-Cl1	105.45(11)	N1-Ni-Cl2	109.97(10)
N4-Ni-Cl1	103.90(11)	N4-Ni-Cl2	113.20(11)
Ni-N1-C7	126.7(3)	Ni-N4-C12	124.8(3)
C1-N1-C7	120.7(4)	C6-N4-C12	122.5(3)
N1-C7-N2	119.7(4)	N4-C12-N5	119.6(4)
N1-C7-N3	124.8(4)	N4-C12-N6	123.8(4)

(The structure of the corresponding bromo complex [(btmgb)$NiBr_2$] is shown in Figure S2a of the Supporting Information, and corresponding parameters are listed in Table S2a of the Supporting Information.) The Ni–N and Ni–Cl bond lengths at 200 K were determined to be 2.000(4)/1.993(3) and 2.2547(15)/2.2436(13) Å, respectively. These values are in line with those obtained previously for related complexes. Thus, for example, in a recently synthesized Ni^{II} complex, in which two bipyridine units attached to a calix[4]arene are bound to $NiCl_2$ fragments, Ni–N and Ni–Cl lengths of 2.003(4)/2.010(4) and 2.180(2)/2.240(1) Å were reported.[22] With 1.310(5) and 1.327(5) Å, the N1–C7 and N4–C12 double bonds are only marginally elongated with respect to the values in the free btmgb ligand (1.2996(16) and 1.2910(16) Å).[17] However, due to the insufficiencies of the standard (promolecule) X-ray model, bond lengths might be biased by both bonding effects as well as the thermal smearing of the charge density. To derive more precise structural parameters for the benchmark system [(btmgb)$NiCl_2$], we therefore performed multipolar refinements based on low-temperature (7 K) high-resolution X-

 © 2010 Wiley-VCH Verlag GmbH & Co. KGaA, Weinheim

ray data (see below and Table 6) thus deconvoluting thermal smearing from chemical bonding effects in the charge-density maps. The obtained highly precise bond lengths of 1.3245(7) and 1.3266(7) Å confirm the double-bond character of the N1–C7 and N4–C12 bonds, respectively, which are approximately 0.12–0.13 Å shorter than the corresponding terminal $N-CH_3$ single bonds of the guanidine ligand (1.4443(7)–1.4573(7) Å). In contrast to $[Ni(^{F}sbqdi)_2]$ or $[Ru(bqdi)(PPh_3)_2(MeCN)_2](PF_6)_2$, which represent typical NIL reference systems, only a subtle shortening of the C2–C3/C4–C5 bond lengths (1.3922(8)–1.3928(8) Å) relative to the remaining C–C bonds of the C_6 ring (1.3958(8)–1.4104(8) Å) could be identified. Hence, the typical (semi)-benzoquinonediimine-type electron distribution of these NIL systems appears to be hindered in $[(btmgb)NiCl_2]$, which is in line with rather long C_{benzyl}–N bond lengths (C1–N1 = 1.4118(7) and C6–N4 = 1.4072(7) Å). These distances are close to the ones of the innocent ligand reference system $(Et_4N)_2[W^0(CO)_3(opda)]$,[23] which range from 1.372(6) to 1.418(6) Å. Furthermore, the six C–N bonds attached to the central guanidine carbon atoms display rather equal distances (C7–N: 1.3245(7)–1.3619(7) and C12–N: 1.3266(8)–1.3611(8) Å). This indicates a pronounced π-electron delocalization inside the guanidine moieties.

We note, however, that the position of the Ni atom is found 0.65 Å away from the phenylene ring plane. This remarkable structural detail clearly discerns $[(btmgb)NiCl_2]$ from the corresponding diamagnetic and approximately square-planar $[(btmgb)PtCl_2]$ complex with the Pt atom lying in the phenylene ring plane.[20] This dislocation of the metal atom in $[(btmgb)NiCl_2]$ is a consequence of the envelope-type ring puckering of the five-membered metallacycle (Ni,N1,C1,C6,N4), which displays a pronounced interplanar angle of 18.26(3)° between the N1,C1,C6,N4 and N1,Ni,N4 entities. Furthermore, the angle between the phenylene ring plane and the (N1,C1,C6,N4) moiety (5.21(3)°) also contributes to the observed dislocation of the central nickel atom. As anticipated, the N-M-N bite angle is larger for M = Ni (83.41(2)°) than for M = Pt (80.6(2)°), but is still relatively small. On the contrary, the Cl-Ni-Cl angle is remarkable large (131.97(1)°) and clearly deviates from the corresponding one in the diamagnetic Pt complex (88.96(6)°) with an approximate square-planar metal coordination. The local symmetry at the Ni atom is thus approximately C_{2v} with a small deviation of the interplanar (Cl1,Ni,Cl2)/(N1,Ni,N4) angle from 90° (87.58(2)°). Through a detailed magnetic susceptibility study, we will later show that the structural peculiarities of $[(btmgb)NiCl_2]$ and related Ni–guanidine complexes (vide infra) are most likely not a signature of the potential non-innocent character of the guanidine ligand but result from a mixing of excited states into the ground state.

$[(btmgn)NiX_2]$: The bisguanidine btmgn represents an example of a kinetically active proton sponge.[18] Proton sponges exhibit a very high affinity towards protons, but are otherwise generally not nucleophilic. Indeed, to date just one complex[24] of the archetypical proton sponge 1,8-bis(dimethylamino)naphthalene[25] has been reported.[26] Recently, some of us synthesized the first examples of transition-metal complexes of btmgn, namely, $[(btmgn)PdCl_2]$ and $[(btmgn)PtCl_2]$, as well as $[(btmgn)PtCl_2(C_2H_4)]$, in which only one of the N atoms of btmgn is bound to the Pt atom.[21] It turned out that btmgn can also be used as a ligand in Ni complexes. Figure 2 illustrates the molecular

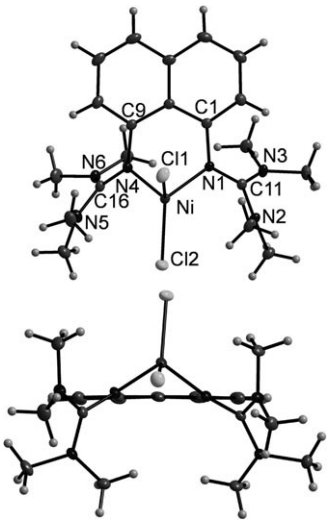

Figure 2. Molecular structure of $[(btmgn)NiCl_2]$. Ellipsoids are drawn at the 50% probability level.

structure of the $[(btmgn)NiCl_2]$ complex and Table 2 contains selected structural parameters. The molecular structure and parameters for the corresponding bromo complex are again provided in the Supporting Information (Figure S2b and Table S2b). The N-Ni-N angle amounts to only 89.69(4)°. Although this value is much smaller than the tetrahedral angle, the Cl-Ni-Cl angle of 128.256(14)° is much larger, a situation that parallels that found for $[(btmgb)NiCl_2]$. It is worth comparing the structure with those of its heavier homologues $[(btmgn)PdCl_2]$ and $[(btmgn)PtCl_2]$.[21] As anticipated, the Pd and Pt homologues feature a planar coordination around the Group 10 metal,

Table 2. Selected parameters (bond lengths [Å] and angles [°]) as determined by X-ray diffraction for $[(btmgn)NiCl_2]$ at 200 K.

Ni–N1	1.9771(10)	Ni–N4	1.8942(10)
Ni–Cl1	2.2610(4)	Ni–Cl2	2.3396(4)
N1–C1	1.4501(14)	N4–C9	1.4437(15)
N1–C11	1.3383(14)	N4–C16	1.3427(15)
C11–N2	1.3297(14)	C16–N5	1.3571(15)
C11–N3	1.3459(14)	C16–N6	1.3164(15)
N1-Ni-N4	89.69(4)	Cl1-Ni-Cl2	128.256(14)
C1-N1-Ni	118.53(7)	C9-N4-Ni	118.41(7)
N1-Ni-Cl1	101.16(3)	N1-Ni-Cl2	115.54(3)
N4-Ni-Cl1	105.79(3)	N4-Ni-Cl2	109.39(3)
Ni-N1-C11	120.61(8)	Ni-N4-C16	119.40(8)
C1-N1-C11	120.80(9)	C9-N4-C16	122.02(9)
N1-C11-N2	119.59(10)	N4-C16-N5	122.15(10)
N1-C11-N3	125.40(10)	N4-C16-N6	120.98(11)

 © 2010 Wiley-VCH Verlag GmbH & Co. KGaA, Weinheim

whereas Ni prefers a distorted tetrahedral coordination. A remarkable detail of the structures of [(btmgn)$PdCl_2$] and [(btmgn)$PtCl_2$] is the nonplanarity of the naphthyl aromatic system. In clear contrast to its Pd or Pt homologue, [(btmgn)$NiCl_2$] features a planar aromatic naphthyl system. The N-Pd-N (81.92(19)°) and N-Pt-N (82.06(12)°) bite angles are identical in the range of the experimental errors and clearly smaller than the one in the third-row congener [(btmgn)$NiCl_2$] (N-Ni-N = 89.69(4)°).

[(btmgbp)NiX_2]: Finally, the complexes [(btmgbp)NiX_2] (X = Cl, Br) were prepared. The molecular structure is depicted in Figure 3 for the chloro derivative (and in Figure S2c of the Supporting Information for the bromo derivative) and selected parameters can be found in Table 3 (and Table S2c of the Supporting Information). Both molecules feature a seven-membered ring. One of the most remarkable structural characteristics is the large X-Ni-X angle of 140.34(3)° (chloro complex) and 145.00(3)° (bromo complex). Quantum chemical calculations on isolated molecules are—except for the salient X-Ni-X angles—in good agreement with the structures in the crystalline phase obtained by X-ray diffraction (see the Supporting Information). We also report herein on the first structural analysis of the free btmgbp ligand. The molecular structure and the corresponding parameters are displayed in Figure S3 and Table S3 of the Supporting Information. The C=N double bonds (N1=C13 and N4=C18) in this compound measure 1.288(2) and 1.286(2) Å and are thus, as anticipated, significantly shorter than the C–N single bonds covering the range 1.377(2)–1.386(2) Å. With measurements of −21.69(30) and −22.54(30)°, the torsional angles C1-N1-C13-N2 and C8-N4-C18-N6 deviate significantly from 0°, which would allow optimal N=C π interaction. Steric reasons are most likely the dominating factors. Finally, the C1-C6-C7-C8 torsional angle between the two phenyl rings amounts to 125.73(20)°. As anticipated, the coordination leads to an increase of the N1–C13 and N4–C18 bond lengths and a decrease of all other N–C bond lengths within the guanidino groups.

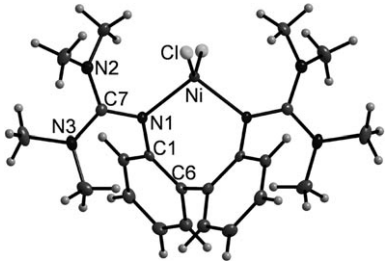

Figure 3. Molecular structure of [(btmgbp)$NiCl_2$]. Ellipsoids are drawn at the 50% probability level.

Table 3. Selected parameters (bond lengths [Å] and angles [°]) as determined by X-ray diffraction for [(btmgbp)$NiCl_2$] at 200 K.

Ni–N1	1.9783(14)	Ni–Cl	2.2599(5)
N1–C1	1.425(2)	N1–C7	1.327(2)
C7–N2	1.360(2)	C7–N3	1.360(2)
C1–C6	1.399(2)	C6–C6′	1.504(3)
N1-Ni-N1′	104.38(8)	Cl-Ni-Cl′	140.34(3)
Ni-N1-C1	114.51(11)	C7-N1-Ni	126.37(12)
N1-C1-C6	121.36(15)	N1-C7-N2	121.06(15)
N1-C7-N3	123.36(16)	N2-C7-N3	115.57(16)
Ni-N1-C7-N2	22.02(46)	Ni-N1-C7-N3	−158.23(26)
C1-C6-C6′-C1′	−67.35(47)		

NMR spectroscopy: We performed various variable-temperature (VT) NMR spectroscopy experiments (with modified recording parameters), which indeed proved to be fruitful. However, the interpretation of these experiments is complicated because of the coincidence between paramagnetic shift and signal splitting due to several fluxional processes within the guanidino groups. We will therefore report on these temperature-dependent studies separately. Herein, we will only report on the two btmgbp complexes [(btmgbp)$NiCl_2$] and [(btmgbp)$NiBr_2$], which gave well-resolved paramagnetic NMR spectra even at room temperature. Figure 4 displays the ^{1}H NMR spectra recorded at 600 MHz for these two complexes at a temperature of

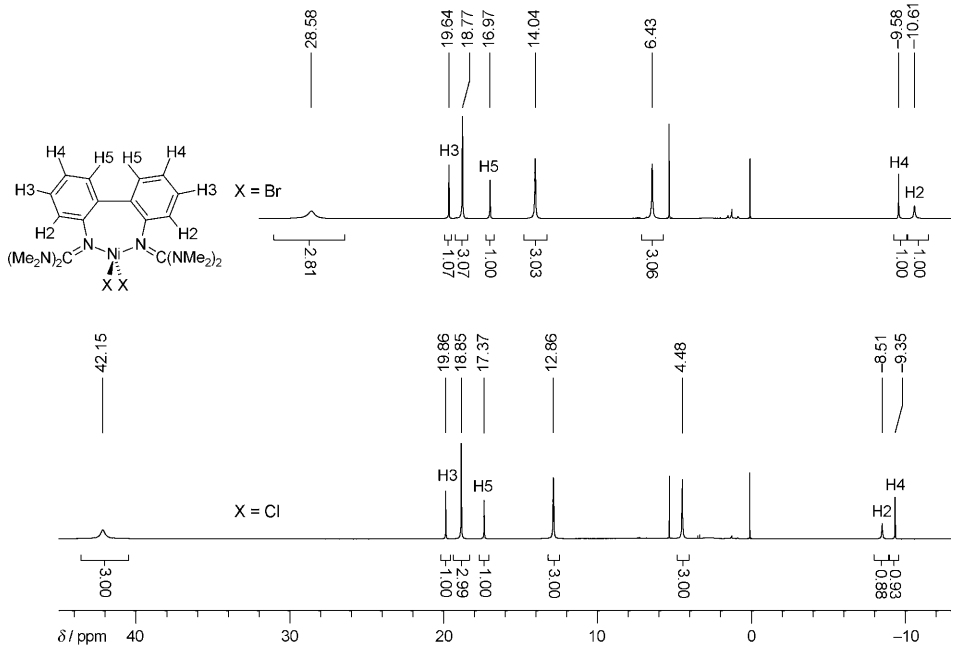

Figure 4. ^{1}H NMR spectra (600 MHz, CD_2Cl_2) as recorded for [(btmgbp)$NiCl_2$] and [(btmgbp)$NiBr_2$].

© 2010 Wiley-VCH Verlag GmbH & Co. KGaA, Weinheim

295 K. Due to their C_2 symmetry, a total of eight signals is expected in both spectra, whereas almost all signals are located outside the diamagnetic region ($\delta = 0$–10 ppm). Integration allows for the separation of the resonances into signals from methyl and from aromatic protons. Furthermore, the assignment of the aromatic protons was realized by considering typical features of the electron–nucleus interactions in paramagnetic compounds.[27] The line broadening associated with the dipolar shift is proportional to the distance between the paramagnetic center and the observed nucleus. Therefore it was assumed that the very broad signal at $\delta = -8.51$ for the chloro and $\delta = -10.61$ for the bromo complex, respectively, corresponds to the aromatic proton closest to the metal center (H2). As the sign of the spin polarization caused by Fermi contact interaction alternates with the number of bonds between the metal center and the H atoms, the second signal with a positive contact shift at $\delta = -9.35$ for the chloro and $\delta = -9.58$ for the analogue bromo complex was assigned to H4. The remaining two signals of aromatic protons (H3, H5), which undergo a negative contact shift, could be distinguished by using 2D NMR spectroscopy experiments. Due to very similar through-space distances to the metal center and identical numbers of bonds between the hydrogen atoms and Ni, a clear assignment of the methyl signals was impossible.

Magnetic measurements: In Figure 5, the inverse magnetic direct-current (dc) susceptibility $\chi^{-1}(T)$ for a selected sample of [(btmgb)$NiCl_2$] is depicted. Here the molar core diamagnetism of $\chi_{dia} = -0.136$ memu mol^{-1} has been subtracted from the data.[28] A linear temperature dependence of $\chi^{-1}(T)$ is observed above 50 K and a fit according to a Curie–Weiss law yields an effective magnetic moment of $\mu_{eff} = 3.12\,\mu_B$, thereby indicating a triplet ground state of

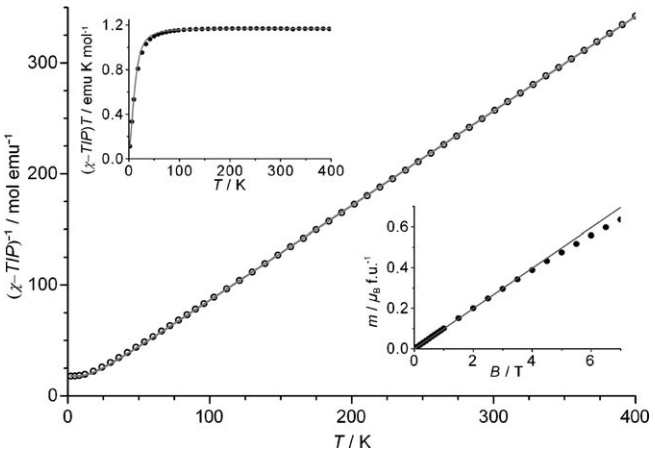

Figure 5. The temperature dependence of the inverse magnetic susceptibility $(\chi - TIP)^{-1}$ and $(\chi - TIP)T$ (see inset in the upper left corner) of [(btmgb)$NiCl_2$] measured in an applied field of $B = 1$ T. In both cases, the solid lines follow a fit to the data according to Equation (3). The magnetic field dependence of the magnetization at $T = 2$ K is depicted in the inset in the lower right corner. Here, the slope of the straight line is equal to $\chi_{sat} = 0.0555$ emu mol^{-1} below 6 K.

[(btmgb)$NiCl_2$],[29a] which is also in line with the predictions by DFT calculations (Table 4).

Below 25 K the inverse susceptibility $\chi^{-1}(T)$ of [(btmgb)$NiCl_2$] starts to deviate from the linear behavior expected for a Curie–Weiss law and saturates below 6 K. Accordingly, the effective magnetic moment $\mu_{eff} \propto \chi T$ displays a constant value at higher temperatures and a rapid decrease below 50 K (see inset on the upper left corner of Figure 5). This observation may be due to an onset of antiferromagnetism (afm). However, the shape of the magnetization curve $m(B)$, pictured in the lower right inset of Figure 5, is in contrast to this scenario, in which a positive curvature of $m(B)$ would be expected.

Table 4. Triplet–singlet energy (ΔE_{TS}) and Gibbs free energy (ΔG_{TS}) differences [kJ mol^{-1}] as calculated for all of the bisguanidine complexes (see the Computational Methods in the Experimental Section).

	ΔE_{TS}	ΔG_{TS}
[(btmgb)$NiCl_2$]	43.3	55.3
[(btmgb)$NiBr_2$]	79.5	88.9
[(btmgn)$NiCl_2$]	133.1	138.0
[(btmgn)$NiBr_2$]	134.5	139.2
[(btmgbp)$NiCl_2$]	103.9	107.2
[(btmgbp)$NiBr_2$]	104.7	100.8

The observed temperature dependency of μ_{eff} can instead be explained by a model that includes the effect of zero-field splitting, that is, the separation of multiplet sublevels in the absence of an external magnetic field.[29b] In this model, the following Hamiltonian is taken as a starting point [Eq. (2)]:[30]

$$\mathscr{H} = D \cdot \left(\boldsymbol{S}_Z^2 - \frac{1}{3}\boldsymbol{S}^2 \right) + \frac{\mu_B g}{\mu_0}(B_0 \cdot \boldsymbol{S}) \qquad (2)$$

in which D is the axial zero-field splitting parameter, $\boldsymbol{S}$ is the spin operator, μ_B is Bohr magneton, μ_0 is the vaccum permeability is the isotropic Landé factor, and B_0 is the external applied magnetic field. In the case of a ground state with quenched orbital moment L and $J = S = 1$, one obtains the following equation for the molar susceptibility [Eq. (3)].[30]

$$\chi_M = \frac{2N_A\mu_B^2}{3k_B(T - \Theta_{CW})} g^2 \frac{e^{-D/k_BT} + 2\frac{k_BT}{D}\left(1 - e^{-D/k_BT}\right)}{(1 + 2e^{-D/k_BT})} + TIP \qquad (3)$$

in which N_A is Avogadro's number, k_B is the Boltzmann constant, Θ_{CW} is the Curie–Weiss temperature (applied to take possible intermolecular interactions into account), and TIP is the temperature-independent paramagnetism. The solid lines in Figure 5 (with the exception of the straight line in the lower right inset) are fitted to the data according to Equation (3). The resulting values for the fit parameters g, D, TIP, and Θ_{CW} are listed in Table 5 (as well as section S16 in the Supporting Information) for all four of the com-

 © 2010 Wiley-VCH Verlag GmbH & Co. KGaA, Weinheim

Table 5. The calculated fit parameters g, D, TIP, and Θ_{CW} obtained by a fit to the inverse susceptibility data $(\chi(T)-TIP)^{-1}$ according to Equation (3). All samples were measured in a magnetic field of 50 mT, except for [(btmgb)$NiCl_2$], which was measured in an applied field of 1 T.

	[(btmgb)$NiCl_2$]	[(btmgb)$NiBr_2$]	[(btmgbp)$NiCl_2$]	[(btmgbp)$NiBr_2$]
g	2.16	2.13	2.21	2.20
D [cm^{-1}]	29.2	29.6	12.7	20.8
TIP [memu mol^{-1}]	0.31	1.09	1.15	0.20
Θ_{CW} [K]	−0.01	−0.01	−0.01	−0.01

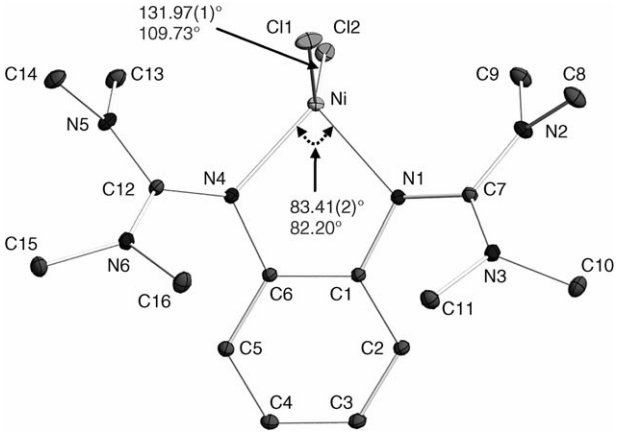

Figure 6. Molecular structure of [(btmgb)$NiCl_2$] based on high-order X-ray data at 7 K and multipolar refinements; 50% probability ellipsoids; hydrogen atoms have been omitted for clarity; selected angles are shown (above: experimental values, below: theoretical values obtained at the PBEPBE/6-311+G(d,p) level of approximation).

pounds. A negligible paramagnetic Curie–Weiss temperature $\Theta_{CW} = -0.01$ K is found for all samples. The values of the isotropic Landé factor g and the axial zero-field splitting parameter D are in good agreement with other studies on tetrahedrally coordinated Ni^{II} complexes, in which the zero-field splitting was taken into account.[30–32]

Electronic structure of [(btmgb)$NiCl_2$]: The origin of zero-field splitting (ZFS) lies in a weak interaction of the spins mediated by spin–orbit coupling.[30] Accordingly, spin–orbit mixing of certain excited states into the ground state of our d^8 Ni–guanidine benchmark system [(btmgb)$NiCl_2$] will influence its electronic structure and consequently its electron-density distribution. Experimental electron-density maps of [(btmgb)$NiCl_2$] should therefore provide hints to the presence of ZFS. In this respect, experimental charge-density studies might complement the established techniques,[30] for example, electron paramagnetic resonance (EPR) spectroscopy, magnetic susceptibility and magnetization measurements, calorimetry, inelastic neutron scattering (INS), and nuclear magnetic relaxation dispersion to characterize the ZFS. Since experimental charge-density distributions do not suffer from an insufficient treatment of relativistic effects and electron correlation, they might serve as reference densities for theoretical studies.[33] Finally, the analysis of the topology of our experimental charge-density distribution of [(btmgb)$NiCl_2$] will allow for the quantification of electron donation from the btmgb ligand to the Ni atom and thus an estimate of the degree of any competing NIL behavior in this benchmark system.

Figure 6 shows an ORTEP plot of [(btmgb)$NiCl_2$] displaying 50% probability ellipsoids based on high-order X-ray data at 7 K and subsequent multipolar refinements. A comparison of the structural parameters of the experimental (at 7 K) and DFT-optimized structure of [(btmgb)$NiCl_2$] (see Table 6 and Figure 6 for salient bond lengths and angles; for further geometrical data, see section S8 of the Supporting Information) shows no major disagreement except in case of the ∢Cl-Ni-Cl valence angles. Although DFT calculations predict a nearly ideal tetrahedral ∢Cl-Ni-Cl angle of 109.7°, a significantly more obtuse angle of 131.973(6)° is found in our experimental model.[34] However, the DFT optimizations of a second [(btmgb)$NiCl_2$] model with the ∢Cl-Ni-Cl angle constrained at the experimental geometry show that the energy increases solely by about 3 kJ mol^{-1} without any further significant consequences to the remaining structural parameters. In the case of MP2 calculation using the respective DFT geometries and the same basis set, an even smaller energy difference is computed (1.9 kJ mol^{-1}). This result suggests a rather soft potential for ∢Cl-Ni-Cl angle distortions, which might be a consequence of the mixing of certain excited states into the ground state due to the ZFS. Differences in experimental and theoretical ∢X-Ni-X valence angles of approximately 15° in combination with a remarkable flatness of the potential-energy surface regarding the variation of this angle were also found for [(btmgb)$NiBr_2$]. Similar but somewhat smaller deviations were also found for the btmgbp analogues (see section S4 of the Supporting Information), and all of these complexes show a significant ZFS (Table 5). This systematic trend in [$LNiX_2$] d^8 complexes that display different bisguanidine (L) and halide ligands (X) suggests that electronic effects (ZFS) rather than intermolecular hydrogen bonding and crystal-packing effects might be responsible for the disagreement between the experimental and DFT-based ∢X-Ni-X valence angles. Indeed, in a recent systematic DFT study of the ZFS in Mn^{II} complexes, Zein et al. demonstrated that "even minor errors in the computed structure by DFT translate into significant errors in the predicted ZFS (by means of the coupled-perturbed spin–orbit coupling approach) owing to the subtle interplay of factors that contribute to the ZFS".[35] Hence, in the study by Zein et al. the quality of the predicted ZFS parameters decreased markedly for the DFT-optimized structures. This again suggests that a proper theoretical treatment of spin–orbit coupling (SOC), the mixing of excited states with the ground state, and eventually also direct dipole–dipole interactions of unpaired electrons (SS)[36] might be necessary for meaningful geometry optimizations of compounds that display a pronounced ZFS. This aspect warrants further exploration in future theoretical studies of our model systems.

To rule out a competing NIL effect in our benchmark [(btmgb)$NiCl_2$], we compared in the first step the topologi-

 © 2010 Wiley-VCH Verlag GmbH & Co. KGaA, Weinheim

Table 6. Comparison of selected experimental and theoretical bond lengths and topological parameters of the electron-density distribution at the BCPs of [(btmgb)$NiCl_2$] and the free btmgb ligand (DFT values only).

Unit	Method	Bond length [Å]	$\rho(r_c)$ [e Å^3]	$\nabla^2\rho(r_c)$ [e Å^5]	ε
Ni–Cl1	exptl	2.2563(2)	0.54(1)	6.3(1)	0.05
	theory[a]	2.283	0.47	4.8	0.03
	theory[b]	2.268	0.49	5.2	0.03
Ni–Cl2	exptl	2.2468(2)	0.56(1)	7.0(1)	0.09
	theory[a]	2.211	0.56	6.0	0.07
	theory[b]	2.201	0.59	6.2	0.05
Ni–N1	exptl	1.9961(4)	0.56(2)	6.7(1)	0.10
	theory[a]	2.010	0.58	8.7	0.06
	theory[b]	2.005	0.59	8.3	0.06
Ni–N4	exptl	1.9888(5)	0.60(1)	8.9(1)	0.14
	theory[a]	2.011	0.58	8.7	0.06
	theory[b]	2.005	0.59	8.3	0.06
N1–C1	exptl	1.4117(7)	1.97(6)	−15.9(2)	0.16
	theory[a]	1.405	1.95	−18.6	0.09
	theory[b]	1.400	2.00	−18.9	0.10
free btmgb	theory[a]	1.399/1.406	1.98/1.96	−19.3/−19.0	0.05
C1–C6	exptl	1.4105(7)	2.15(4)	−22.3(1)	0.22
	theory[a]	1.424	1.98	−18.3	0.23
	theory[b]	1.419	2.03	−19.4	0.23
free btmgb	theory[a]	1.430	1.93	−17.3	0.23
C1–C2	exptl	1.3999(7)	2.08(5)	−18.9(2)	0.19
	theory[a]	1.408	1.99	−18.4	0.22
	theory[b]	1.405	2.04	−19.3	0.20
free btmgb	theory[a]	1.411	1.98	−18.1	0.23
C2–C3	exptl	1.3922(8)	2.07(5)	−17.3(2)	0.12
	theory[a]	1.395	2.02	−18.9	0.21
	theory[b]	1.394	2.07	−19.9	0.19
free btmgb	theory[a]	1.399	2.02	−19.0	0.21
C3–C4	exptl	1.3958(8)	2.21(4)	−25.0(1)	0.17
	theory[a]	1.401	2.02	−19.0	0.20
	theory[b]	1.397	2.07	−19.7	0.18
free btmgb	theory[a]	1.401	2.02	−19.0	0.20
N1–C7	exptl	1.3245(7)	2.58(7)	−30.3(3)	0.30
	theory[a]	1.337	2.29	−23.6	0.21
	theory[b]	1.333	2.37	−25.3	0.22
free btmgb	theory[a]	1.303/1.301	2.44	−24.6/−24.7	0.25/0.26
C7–N2	exptl	1.3555(7)	2.26(6)	−18.4(3)	0.22
	theory[a]	1.369	2.12	−21.2	0.23
	theory[b]	1.365	2.19	−22.9	0.25
N2–C8	exptl	1.4497(7)	1.79(6)	−15.8(3)	0.13
	theory[a]	1.462	1.72	−20.5	0.23
	theory[b]	1.458	1.75	−14.7	0.06

[a] PBEPBE/6-311+G(d,p) level of approximation. [b] PBE-ZORA/TZ2P level of approximation.

cal properties of the C–C bonds at their bond critical points (BCPs). For detailed information, see section S11 in the Supporting Information. Despite the minute shortening of the C2–C3/C4–C5 bonds relative to the remaining C–C bonds of the benzyl ring, the topological parameters do not support any benzoquinonediimine-type electron distribution in favor of an NIL behavior. Indeed, the slightly shortened C2–C3/C4–C5 bonds display a smaller charge density accumulation at the bond critical points $\rho(r_c) = 2.07(5)$ e Å^{-3} relative to the somehow elongated C3–C4/C1–C6 bonds $\rho(r_c) = 2.21(4)$ e Å^{-3} (see Table 6). However, these differences are small, and the two-dimensional representation of the Laplacian, $\nabla^2\rho(r)$, in the phenyl plane (Figure 7) shows similar charge concentration and depletion features in the valence shell of all carbon atoms. This again rules out any significant distortions of the phenyl ring π system and rather disfavors the classification of the btmgb donor molecule as a non-innocent ligand in [(btmgb)$NiCl_2$].

In the next step we inspected the local electronic situation at the complex center. The salient topological properties of the Ni–N and Ni–Cl bonds are again reported in Table 6. The positive sign of the Laplacian and the significant density accumulation (ca. 0.6 e Å^{-3}) at the Ni–N BCPs reflect the high polarity of these covalent Ni–N bonds. Since strong Ni–N1/Ni–N4 bonds are presumably established at the expense of their neighboring N1–C7/N4–C12 bonds, one would expect that the formal double-bond character of these bonds is significantly reduced relative to the situation in the free btmgb ligand. This shortening is, however, only weakly reflected by the N1–C7/N4–C12 bond-length differences between the free and coordinated btmgb ligand (see above and Table 6). We therefore traced bond ellipticity (ε) profiles[37] of the characteristic N–C bonds in [(btmgb)$NiCl_2$] as sensitive measure of their π-bonding character. According to the mathematical definition (Figure 8), ε values greater than zero indicate partial π character in a bond or electronic distortion from σ symmetry along the bond path. Whereas the ellipticity profile of ethene shows a symmetrical bell-shaped ellipticity profile around the BCP,[37a] the DFT calculations predict rather asymmetric ε profiles for the polar C7–N1 bond in the free btmgb ligand (Figure 8). This is mainly due to a significant shift of the BCP towards the more electropositive carbon atom.[38b,c] The computed ellipticity at the BCP of 0.25 for the btmgb ligand is pronounced and serves as our benchmark for a localized N=C double bond. On complexation, however, the calculated bond ellipticity and thus the double-bond character becomes clearly reduced ($\varepsilon = 0.21$), which is in line with a subtle bond elongation of approximately 0.03 Å. More remarkable, however, is the formation of a second maximum in the C7–N1 ellipticity profile of [(btmgb)$NiCl_2$]. This apparent additional perturbation of the valence density[38a,d,e] is connected to the fine structure of the valence shell of charge concentra-

 © 2010 Wiley-VCH Verlag GmbH & Co. KGaA, Weinheim

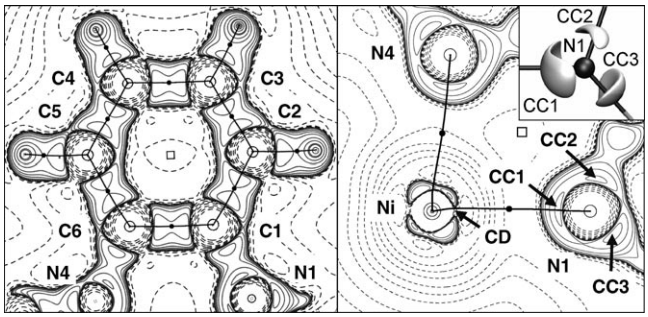

Figure 7. Contour map of $L(\boldsymbol{r}) = -\nabla^2\rho(\boldsymbol{r})$ in the plane spanned by the phenyl ring (left) and in the (Ni,N1,N4) plane (right) in [(btmgb)$NiCl_2$] obtained from the experimentally determined charge-density distribution. Contour levels are drawn at 0, $\pm(2.0\times10^n)$, $\pm(4.0\times10^n)$, $\pm(8.0\times10^n)$ e Å^{-5}, in which $n=0, \pm3, \pm2, \pm1$; positive and negative values are marked by solid and dashed lines, respectively. Solid lines denote the bond paths. BCPs and ring critical points (RCPs) are marked by closed circles and open squares, respectively. The inset on the right-hand side displays the envelope map of $L(\boldsymbol{r})$ at the N1 atom in [(btmgb)$NiCl_2$]. In the case of the nitrogen donor atom N1, three bond-directed valence charge concentrations (CC1–CC3) are denoted by arrows. Note that CC1 of the nitrogen donor atoms points to a local charge depletion zone (CD) at the nickel atom in a key-and-lock principle.

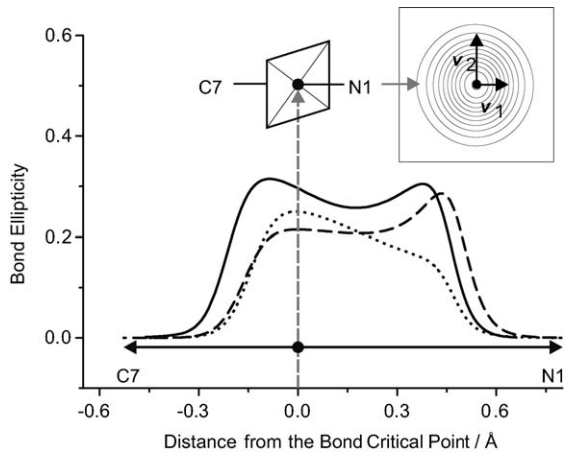

Figure 8. Experimental (——) and theoretical (PBEPBE/6-311+G(d,p) level of approximation) bond ellipticity profiles along the N1–C7 bond in [(btmgb)$NiCl_2$] (– – –) and the free btmgb ligand (•••••). The definition of the bond ellipticity (ε) is illustrated by the $\rho(\boldsymbol{r})$ contour map in the inset showing the charge density in the plane perpendicular to the bond path at the C7–N1 bond CP of the free btmgb ligand. Thus, ε is a measure of the nonspherical charge distribution of $\rho(\boldsymbol{r})$: $\varepsilon=\lambda_1/\lambda_2-1$. λ_i are the eigenvalues of the corresponding eigenvectors $\boldsymbol{v}_1$ and $\boldsymbol{v}_2$ of the Hessian matrix of $\rho(\boldsymbol{r})$.

tion[39] (VSCC) of the N1 atom as we will see later (Figure 7). We note that the N1–C7 ellipticity profile based on the experimental data shows slightly higher ellipticity values; however, both profiles display the same characteristic double-maximum topology, which clearly differs from that in the free btmgb ligand.

To quantitatively survey the actual donor capability of the btmgb ligand, the values of the atoms-in-molecules (AIM) atomic charge q_B and the integrated source function SF($\boldsymbol{r}',\Omega$)[40] are listed in Table 7. In case of the formally d^8-con-

Table 7. Atomic charges and integrated source function SF($\boldsymbol{r},\Omega$) of the Ni–N1 BCP resulting from integration of the experimentally and theoretically obtained charge-density distribution (PBEPBE/6-311+G(d,p) level of approximation) over atomic basins in [(btmgb)$NiCl_2$]. For a complete list, see sections S13 and S14 of the Supporting Information.

Basin	Method	q_B [e]	SF of Ni–N1 BCP [% of $\rho(\boldsymbol{r}_c)$]
Ni	exptl	+0.859	35.3
	theory	+0.913	37.7
Cl1	exptl	−0.818	4.5
	theory	−0.622	3.8
Cl2	exptl	−0.723	4.4
	theory	−0.619	4.3
N1	exptl	−1.103	24.1
	theory	−1.079	26.3
N4	exptl	−1.091	−0.6
	theory	−1.079	−0.7
benzyl moiety	exptl	+0.677	13.4
	theory	+0.637	11.6
guanidine 1[a]	exptl	+0.025	38.8
	theory	−0.145	38.9
guanidine 2[a]	exptl	+0.037	5.7
	theory	−0.143	4.6

[a] The guanidine 1 unit is defined as the following group of atoms: N1–N3, C7–C11, and the hydrogen atoms bonded to these carbon atoms. The guanidine 2 unit is likewise defined by the atoms N4–N6, C12–C16. Integrated charges (q_B [e]) in the free btmgb ligand (PBEPBE/6-311+G(d,p)): N1: −1.102; N4: −1.080; benzyl moiety: +0.581; each guanidine moiety: −0.281.

figured Ni atom, we find net charges of +0.86 and +0.91 e, which are in fine agreement between experiment and theory, respectively. This large deviation from its formal charge is further support for pronounced Ni←N donation. The net charges of the two chlorine atoms (−0.82/−0.72 e [both −0.62 e]) are close to their expected formal charge of −1 (theoretical values are specified in square brackets in the following). To gain a more detailed insight into the charge transfer between the metal center and its ligand, the integrated source function SF($\boldsymbol{r}',\Omega$) was calculated for the Ni–N BCPs in the next step. Making use of Green's function, the SF($\boldsymbol{r}',\Omega$) provides a measure of the relative importance of the contribution of each atom to the density at a specific reference point $\boldsymbol{r}'$. Furthermore, the source function atomic contributions represent "a more robust chemical bond descriptor than other commonly used bond topological indices which are too sensitive" to the choice of the multipole model in experimental or of the method of approximation in theoretical studies.[40f] As expected, the major contributions to the density at the Ni–N1 bond critical point arise from the atoms constituting the bond (59.4%, (64.0%)). Further significant contributions to the Ni–N1 BCP stem to an almost equal share from the phenyl ring and the C[N-$(CH_3)_2$]$_2$ moiety attached to N1 (13.4% [11.6%] and 14.7% and [12.6%], respectively). Hence, the btmgb ligand clearly acts as a strong electron donor in the presence of the Lewis acidic $NiCl_2$ moiety.

Strong metal–ligand interactions are also signaled by the pronounced structuring of the VSCC at the nitrogen donors and the central Ni atom. Indeed, zones of local charge con-

 © 2010 Wiley-VCH Verlag GmbH & Co. KGaA, Weinheim

centration (CC) and charge depletion (CD) in the VSCC are clearly revealed by local maxima and minima of the negative Laplacian of the electron density $L(\boldsymbol{r}) = -\nabla^2\rho(\boldsymbol{r})$, respectively (Figure 7).[39a] In the case of the coordinating N atoms (see inset of Figure 7, right) two bonding CCs point towards the neighboring carbon atoms (C1/C7 and C6/C12, respectively) and signal covalent N–C bonding. Furthermore, Figure 7 shows that a third CC of each nitrogen donor faces a corresponding CD at the Ni atom in a key-and-lock principle in line with pronounced Ni–N charge transfer. We further note that these metal-directed CCs at the N1 and N4 atoms (denoted CC1 in the inset of Figure 7) extend significantly above and below the NiN_2 plane consonant with the presence of π(N→Ni) donation (see section S17 of the Supporting Information for details). However, the σ(N→Ni) donor component clearly exceeds these π interactions. Therefore, only three equatorial bond-directed charge concentrations (denoted CC1–CC3 in Figure 7) are observed at the N1 and N4 atoms, whereas the formation of spatially separated nonbonding charge concentrations above and below the NiN_2 plane is prevented. From a topological point of view, the diffuse and extended shape of CC1 can be therefore considered to result from a merging of the axial nonbonding valence charge concentrations and the metal-directed lone-pair charge concentration (yielding the σ(N→Ni) donation) at the N1/N4 atoms into a single feature (denoted CC1 in Figure 7). This topological scenario reflects the mixed σ/π character of the Ni–N bond. In contrast, the noncoordinating sp^2-hybridized nitrogen atoms N3 and N6 display spatially resolved axial CCs that are in accordance with a significant π delocalization in the NC_3 moieties[38c] (see section S17 of the Supporting Information). The π-bonding character of the Ni–N bonds is additionally supported by pronounced Ni–N bond ellipticities of 0.10–0.14 [0.06] as well as by the presence of four Kohn–Sham spin orbitals of significant Ni–N π character (see section S15 of the Supporting Information for details). Regarding the VSCC of the central metal atom, we find six local charge depletion zones in an octahedral arrangement, consistently in theory and experiment (see Figure 9, left and middle). However, the choice of higher isosurface $L(\boldsymbol{r})$ values reveals distinct differences between experiment and theory: the latter one displays eight zones of charge concentration versus six zones in our experimental model. These differences might be directly due to the incomplete treatment of spin-orbit mixing

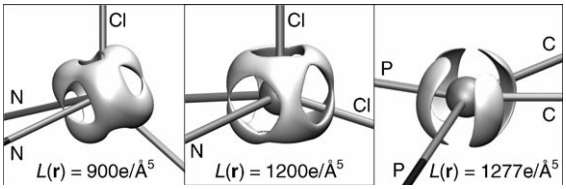

Figure 9. Envelope map of $L(\boldsymbol{r})$ at the Ni atom in [(btmgb)$NiCl_2$] obtained from the experimental (left) and theoretical (middle, PBEPBE/6-311+G(d,p) level of approximation) charge-density distributions, and of the Ni VSCC in [(dbpe)Ni(C_2H_4)], also obtained from an experimental charge-density study (right).

of excited states into the ground state of the molecule in the theoretical model. However, the local $L(\boldsymbol{r})$ topologies in the VSCC of the nickel atom are still highly related and clearly deviate from what is found in the diamagnetic d^{10} complex [(dbpe)Ni(C_2H_4)][41] (dbpe = 1,2-bis(di-*tert*-butylphosphino)-ethane, Figure 9, right). Here, the metal center is coordinated in a square-planar arrangement and the number of CCs—in theory as well as in experimental studies—reduces to four.

In a final step, the spin density of the complex was analyzed; it is depicted in Figure 10. At a first glance, it is already clear that the spin density is virtually concentrated at

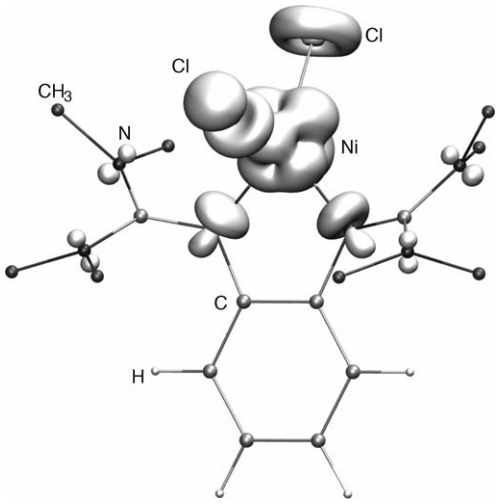

Figure 10. Envelope map of the spin density $\rho_s(\boldsymbol{r}) = 0.005$ au of [(btmgb)$NiCl_2$] (PBE-ZORA/TZ2P level of approximation).

the Cl_2NiN_2 moiety. Integration of the spin density over each atomic basin provides the following atomic spins (PBE-ZORA/TZ2P level of approximation): $q_s(Ni) = 1.51$, $q_s(Cl1) = 0.09$, $q_s(Cl2) = 0.14$, $q_s(N1) = 0.06$, and $q_s(N4) = 0.05$ e. Significantly, smaller spin contaminations (0.02 e) are located at the N atoms of the bisguanidine units (for a detailed list, see section S14 of the Supporting Information), integration of the remaining atomic basins yields only negligible spin contributions. The lack of spin density at the phenyl ring again disfavors the classification of btmgb as a predominant non-innocent ligand and is in good agreement with our conclusions based on structural data and topological analyses of the electron-density distribution. However, we expect a quite different scenario in the case of 1,2,4,5-tetrakis(tetramethylguanidino)benzene complexes, which are characterized by a stronger donor–acceptor character. These complexes will be the focus of future studies.

Conclusion

Herein we used the chelating bisguanidine ligands bis(tetramethylguanidino)benzene (btmgb), bis(tetramethylguanidino)naphthalene (btmgn), and bis(tetramethylguanidino)bi-

 © 2010 Wiley-VCH Verlag GmbH & Co. KGaA, Weinheim

phenyl (btmgbp) to synthesize six new paramagnetic Ni^{II} complexes that exhibit interesting magnetic properties and electronic structures. A detailed inspection of the magnetic susceptibility of [(btmgb)NiX_2] and [(btmgbp)NiX_2] (X = Cl, Br) revealed a linear temperature dependence of $(\chi - TIP)^{-1}$ (T) above 50 K, which was in agreement with a Curie–Weiss-type behavior and a triplet ground state. Below approximately 25 K, however, the inverse susceptibility of [(btmgb)NiX_2] and [(btmgbp)NiX_2] starts to deviate from the Curie–Weiss law and saturates below 6 K. This behavior could be explained by a model that includes the effect of zero-field splitting (ZFS) and thus the spin–orbit mixing of certain excited states into the ground state. The presence of ZFS was identified as one potential reason for the rather flat ∢Cl-Ni-Cl deformation potential and the distinct differences between the ∢X-Ni-X valence angles observed by experiment and predicted by DFT. An analysis of the topology of the experimental and theoretical electron-density distributions of [(btmgb)$NiCl_2$] confirmed the strong donor character of the bisguanidine ligand but clearly ruled out any significant non-innocent ligand (NIL) behavior. Hence, [(btmgb)$NiCl_2$] provides an experimental reference system for studying the mixing of certain excited states into the ground state unbiased by any competing NIL behavior. The detailed evaluation of the electronic structure of the [(btmgb)$NiCl_2$] complex thus provides an innocent benchmark system for future studies on Ni^{II} complexes that display the "non-innocent" ligand 1,2,4,5-tetramethylguanidinobenzene (ttmgb).

Experimental Section

All reactions were carried out under an atmosphere of argon by using standard Schlenck techniques. The bisguanidines btmgb[20,17] and btmgbp[42] were synthesized as described in the literature. The bisguanidine btmgn and [(dme)$NiCl_2$] were purchased from Fluka and ABCR, respectively. Dichloromethane was dried over CaH_2 and distilled before using. Acetonitrile and *n*-hexane were purchased from Aldrich and used without further purification. NMR spectra were recorded using a Bruker Avance III 600 spectrometer. A Perkin–Elmer Lambda 19 and a Tidas II J&M spectrometer were used for UV/Vis spectroscopy. Magnetic measurements were made using a Quantum Design MPMS-XL-5 apparatus or a Quantum Design MPMS-XL-7. For IR spectroscopy CsI discs of the compounds were made, which were then measured using a FTIR Biorad Merlin Excalibur FT 3000 spectrometer. CV measurements were conducted using a EG&G Princeton 273 apparatus.

[(btmgb)$NiCl_2$]: [(dme)$NiCl_2$] (109.9 mg, 0.50 mmol) was dissolved in CH_2Cl_2 (5 mL), cooled to −80 °C, and subsequently added to a solution of btmgb (152.2 mg, 0.50 mmol) in CH_2Cl_2 (10 mL; also cooled to −80 °C). The mixture changed its color gradually to brown. After stirring the suspension for 1 h at −80 °C, the mixture was allowed to warm up to room temperature over 18 h. A green-grey precipitate was filtered off, and the solvent of the filtrate was removed in vacuo. A green precipitate was obtained. It was washed 2 times with *n*-hexane (5 mL). Yield: 188.1 mg (87 %). Crystals suitable for X-ray diffraction were obtained in CH_3CN at 2 °C. IR (CsI): $\tilde{\nu}$ = 2930 (m) (ν(C−H)), 2881 (m) (ν(N−CH_3)), 1634 (s) (ν(C=N)), 1541 (s) (ν(C=N)), 1463 (s), 1399 (s) (δ(C−H)/ν(C=C)), 752 cm^{-1} (s) (δ(C^{aromat}–H)); UV/Vis (CH_2Cl_2, $c = 1.55\times10^{-3}$ mol L^{-1}, 20 °C): λ (ε) = 430 (487.8), 504 (216.6), 570 (125.3), 690 nm (79.2 $mol^{-1}\,dm^3\,cm^{-1}$); HRMS (EI$^+$): m/z (%): 434.1087 (100.00) $[M]^+$, 397.1410 (6.06) $[M-Cl]^+$, 304.2376 (41.93) $[M-Cl_2Ni]^+$, 260.1865 (58.52) $[M-C_2H_6NCl_2Ni)]^+$, 233.1765 (39.62) $[M-C_3H_7N_2Cl_2Ni]^+$, 190.1446 (17.95) $[M-C_5H_{12}Cl_2N_3Ni]^+$, 188.1309 (30.68) $[M-C_5H_{14}Cl_2N_3Ni]^+$; elemental analysis calcd (%) for $C_{16}H_{28}Cl_2N_6Ni$ (413.6): C 44.28, H 6.50, N 19.36; found: C 46.37, H 6.80, N 20.33.

Crystal data for [(btmgb)$NiCl_2$]: $C_{16}H_{28}Cl_2N_6Ni$; M_r = 434.05; 0.35 × 0.35 × 0.20 mm^3; monoclinic; space group $P2_1/n$; a = 14.292(3), b = 10.838(2), c = 14.436(3) Å; β = 113.06(3)°; V = 2057.4(7) $Å^3$; Z = 4; ρ_{calcd} = 1.401 $Mg\,m^{-3}$; $Mo_{K\alpha}$ radiation (graphite monochromated, λ = 0.71073 Å); T = 200 K; θ_{range} = 1.70 to 27.50°; reflections measured 8775; independent reflections 4555; R_{int} = 0.0910; semiempirical absorption correction; final R indices [$I > 2\sigma(I)$]: $R1$ = 0.0558, $wR2$ = 0.1457.

[(btmgb)$NiBr_2$]: A solution of [(dme)$NiBr_2$] (77.2 mg, 0.25 mmol) in CH_2Cl_2 (5 mL) was cooled to −40 °C and added to a solution of btmgb (76.1 mg, 0.25 mmol) in CH_2Cl_2 (10 mL) at −40 °C. After stirring the dark brown-green suspension for 1 h at −40 °C, the mixture was allowed to warm up to room temperature over 18 h. A dark green precipitate was filtered off, and the solvent of the filtrate was removed in vacuo to obtain a dark green precipitate, which was washed 2 times with *n*-hexane (5 mL). Yield: 114.8 mg (88 %). Crystals suitable for X-ray diffraction were obtained in CH_3CN at 2 °C. IR (CsI): $\tilde{\nu}$ = 2930 (m) (ν(C−H)), 2873 (m) (ν(N−CH_3)), 2797, 1690–1500 (s) (ν(C=N)/ν(C=C)), 1399 (s) (δ(C−H)), 770 cm^{-1} (s) (δ(C^{aromat}–H)); UV/Vis (CH_2Cl_2, $c = 1.32\times10^{-3}$ mol L^{-1}, 20 °C): λ (ε) = 457 (421.8), 526 (290.8), 598 (152.5), 707 nm (78.1 $mol^{-1}\,dm^3\,cm^{-1}$); HRMS (EI$^+$): m/z (%): 522.0071 (77.20) $[M]^+$, 443.0910 (100.00) $[M-Br]^+$, 361.1634 (8.90) $[M-HBr_2]^+$, 305.7143 (9.06) $[M-Br_2Ni+H]^+$, 260.1862 (59.31) $[M-C_2H_6NBr_2Ni)]^+$, 233.1746 (30.97) $[M-C_3H_7N_2Br_2Ni]^+$, 188.1316 (46.55) $[M-C_5H_{14}Br_2N_3Ni]^+$; elemental analysis calcd (%) for $C_{16}H_{28}Br_2N_6Ni$ (522.97): C 36.75, H 5.40, N 16.07; found: C 34.98, H 5.40, N 15.26.

Crystal data for [(btmgb)$NiBr_2$]: $C_{16}H_{28}Br_2N_6Ni$; M_r = 522.97; 0.23 × 0.14 × 0.04 mm^3; monoclinic; space group $P2_1/n$; a = 14.214(3), b = 10.840(3), c = 14.616(3) Å; β = 113.110(4)°; V = 2071.4(8) $Å^3$; Z = 4, ρ_{calcd} = 1.677 $Mg\,m^{-3}$; $Mo_{K\alpha}$ radiation (graphite monochromated, λ = 0.71073 Å); T = 200 K; θ_{range} = 1.67 to 31.50°; reflections measured 51930; independent reflections 6847; R_{int} = 0.0657; semiempirical absorption correction; final R indices [$I > 2\sigma(I)$]: $R1$ = 0.0308, $wR2$ = 0.0738.

[(btmgn)$NiCl_2$]: A cooled (−80 °C) solution of [(dme)$NiCl_2$] (109.9 mg, 0.50 mmol) in CH_2Cl_2 (5 mL) was added to a cooled (−80 °C) solution of btmgn (177.3 mg, 0.50 mmol) in CH_2Cl_2 (10 mL). The mixture changed its color to brown. After stirring for 1 h, the mixture was allowed to warm up to room temperature over 18 h. A brown precipitate was filtered off, and the solvent of the filtrate was removed in vacuo to obtain a brown precipitate, which was washed 2 times with *n*-hexane (5 mL). Yield: 127.7 mg (53 %). Crystals suitable for X-ray diffraction were obtained in CH_3CN at 2 °C. IR (CsI): $\tilde{\nu}$ = 2995 (m) (ν(C−H)), 2870 (m) (ν-(N−CH_3)), 1610 (s) (ν(C=N)), 1555 (s) (δ(C=N)), 1465 (s) (δ(C=N)), 1410 (s) (δ(C=C)), 765 cm^{-1} (m) (δ($C^{naphthyl}$–H); UV/Vis (CH_2Cl_2, $c = 2.61\times10^{-4}$ mol L^{-1}, 20 °C): λ (ε) = 409 (2549.1), 530 (427.8), 568 nm (334.8 $mol^{-1}\,dm^3\,cm^{-1}$); HRMS (EI$^+$): m/z (%): 484.1236 (98.92) $[M]^+$, 447.1572 (13.15) $[M-Cl]^+$, 354.2498 (100.00) $[M-Cl_2Ni]^+$, 310.2047 (34.26) $[M-C_2H_6NCl_2Ni]^+$, 283.1918 (43.40) $[M-C_4H_9NCl_2Ni]^+$, 253.1573 (78.77) $[M-C_5H_{13}N_2Cl_2Ni]^+$, 210.1083 (24.37) $[M-C_7H_{18}N_3Cl_2Ni]^+$; elemental analysis calcd (%) for $C_{20}H_{30}Cl_2N_6Ni$ (484.11): C 49.62, H 6.25, N 17.36; found: C 53.72, H 7.20, N 18.79.

Crystal data for [(btmgn)$NiCl_2$]: $C_{20}H_{30}Cl_2N_6Ni$; M_r = 484.11; 0.35 × 0.30 × 0.10 mm^3; monoclinic; space group $P2_1/c$; a = 11.1608(16), b = 11.3948(16), c = 17.825(3) Å; β = 92.423(2)°; V = 2264.9(6) $Å^3$; Z = 4; ρ_{calcd} = 1.420 $Mg\,m^{-3}$; $Mo_{K\alpha}$ radiation (graphite monochromated, λ = 0.71073 Å); T = 200 K; θ_{range} = 1.83 to 31.00°; reflections measured 57358; independent reflections 7145; R_{int} = 0.0308; semiempirical absorption correction; final R indices [$I > 2\sigma(I)$]: $R1$ = 0.0274, $wR2$ = 0.0811.

[(btmgn)$NiBr_2$]: A solution of [(dme)$NiBr_2$] (154.3 mg, 0.50 mmol) in CH_2Cl_2 (5 mL) was cooled to −80 °C and added to a solution of btmgn (177.3 mg, 0.50 mmol) in CH_2Cl_2 (10 mL), which was also cooled to −80 °C. The mixture changed its color to brown. After stirring for 1 h, the mixture was allowed to warm up to room temperature over 18 h. A brown-grey precipitate was filtered off, and the solvent of the filtrate was removed in vacuo to obtain a brown powder. The residue was washed 2

 © 2010 Wiley-VCH Verlag GmbH & Co. KGaA, Weinheim

times with *n*-hexane (5 mL). Yield: 137.3 mg (48%). Crystals suitable for X-ray diffraction were obtained in CH_3CN at 2°C. IR (CsI): $\tilde{\nu}$ = 2918 (m) (ν(C–H)), 2872 (m) (ν(N–CH_3)), 1616 (s) (ν(C=N)), 1543 (s) (ν(C=N)), 1462 (s) (δ(C=N)), 1396 (s) (δ(C=C)), 765 cm^{-1} (m) ($\delta(C^{naphthyl}–H)$); UV/Vis (CH_2Cl_2, $c = 5.97\,10^{-4}$ mol L^{-1}, 20°C): λ (ε) = 428 (1204.0), 533 (304.7), 577 (291.7), 630 nm (134.6 $mol^{-1}\,dm^3\,cm^{-1}$); HRMS (EI$^+$): *m*/*z* (%): 572.0224 (100.00) $[M]^+$, 493.0898 (92.42) $[M–Br]^+$, 411.1783 (6.75) $[M–HBr_2]^+$, 354.2549 (53.76) $[M–Br_2Ni]^+$, 310.1995 (27.85) $[M–C_2H_6NBr_2Ni]^+$, 283.1924 (20.76) $[M–C_4H_9NCl_2Ni]^+$, 253.1571 (37.08) $[M–C_5H_{13}N_2Cl_2Ni]^+$; elemental analysis calcd (%) for $C_{20}H_{30}Br_2N_6Ni$ (573.03): C 41.92, H 5.28, N 14.67; found: C 45.03, H 6.12, N 15.67.

Crystal data for [(btmgn)NiBr$_2$]: $C_{20}H_{30}Br_2N_6Ni$; M_r = 573.03; 0.24 × 0.21 × 0.18 mm^3; monoclinic; space group $P2_1/c$; a = 11.3063(11), b = 11.6281(12), c = 18.0834(18) Å; β = 91.265(2)°; V = 2376.9(4) $Å^3$; Z = 4; ρ_{calcd} = 1.601 $Mg\,m^{-3}$; $Mo_{K\alpha}$ radiation (graphite monochromated, λ = 0.71073 Å); T = 200 K; θ_{range} = 1.80 to 31.50°; reflections measured 58401; independent reflections 7829; R_{int} = 0.0352; semiempirical absorption correction; final R indices [$I > 2\sigma(I)$]: $R1$ = 0.0246, $wR2$ = 0.0665.

[(btmgbp)NiCl$_2$]: A solution of [(dme)$NiCl_2$] (219.7 mg, 1.00 mmol) in CH_2Cl_2 (15 mL) was cooled to −10°C and slowly added to a solution of btmgbp (379.3 mg, 1.00 mmol) in CH_2Cl_2 (40 mL; also cooled to −10°C). Subsequently, the reaction mixture was allowed to warm up to room temperature, which resulted in a color change of the solution from yellow to deep blue. After 18 h stirring at room temperature, the reaction mixture was filtered with a cannula, and the solvent removed in vacuum from the filtrate. The residue was washed 2 times with *n*-hexane (10 mL), thus yielding [(btmgbp)$NiCl_2$] (334.0 mg, 66%) as a purple powder. Crystals suitable for X-ray diffraction were obtained by recrystallization in CH_3CN at 4°C. IR (CsI): $\tilde{\nu}$ = 3449 (br), 3047 (w), 3013 (w), 2938 (br), 2887 (br), 1618 (w), 1536 (s), 1472 (m), 1420 (s), 1394 (s), 1337 (m), 1242 (s), 1217 (br), 1157 (s), 1099 (w), 1066 (w), 1035, 937 (w), 862 (m), 817 (s), 801 (m), 760 (m), 773 (m), 737 (w), 699 (w), 638 (w), 626 (w), 580 (w), 555 (w), 528 (m), 502 (m), 463 cm^{-1} (w); UV/Vis (CH_2Cl_2, $c = 3.03 \times 10^{-3}$ mol L^{-1}, 20°C): λ (ε) = 626 (130.9), 547 nm (200.7 $mol^{-1}\,dm^3\,cm^{-1}$); HRMS (EI$^+$): *m*/*z* (%): 510.1403 (29.00) $[M]^+$, 472.1656 (100.00) $[M–HCl]^+$, 436.1827 (14.66) $[M–2HCl]^+$, 380.2667 (77.40) [btmgp]$^+$; elemental analysis calcd (%) for $C_{22}H_{32}Cl_2N_6Ni$ (510.15): C 51.80, H 6.32, N 16.47; found: C 51.95, H 6.35, N 16.18.

Crystal data for [(btmgbp)NiCl$_2$]: $C_{22}H_{32}Cl_2N_6Ni$; M_r = 510.15; 0.20 × 0.20 × 0.10 mm^3; orthorhombic; space group *Pbcn*; a = 17.159(2), b = 8.6647(10), c = 16.2321(19) Å; V = 2413.3(5) $Å^3$; Z = 4; ρ_{calcd} = 1.404 $Mg\,m^{-3}$; $Mo_{K\alpha}$ radiation (graphite monochromated, λ = 0.71073 Å); T = 200 K; θ_{range} = 2.37 to 27.50°; reflections measured 58320; independent reflections 2772; R_{int} = 0.1005; semiempirical absorption correction; final R indices [$I > 2\sigma(I)$]: $R1$ = 0.0426, $wR2$ = 0.1203.

[(btmgbp)NiBr$_2$]: A solution of [(dme)$NiBr_2$] (84.3 mg, 0.27 mmol) in CH_2Cl_2 (8 mL) was cooled to −10°C and slowly added to a solution of btmgbp (96.8 mg, 0.25 mmol) in CH_2Cl_2 (16 mL; also cooled to −10°C). Subsequently, the reaction mixture was allowed to warm up to room temperature, thereby resulting in a color change of the solution from yellow to light blue. After 1 h stirring at room temperature, the reaction mixture was filtered with a cannula, and the solvent removed in vacuum from the filtrate. The residue was washed 2 times with *n*-hexane (5 mL), thus yielding [(btmgbp)$NiBr_2$] (96.2 mg, 65%) as a purple powder. Crystals suitable for X-ray diffraction were obtained in CH_3CN at 4°C. IR (CsI): $\tilde{\nu}$ = 3422 (br), 3043 (w), 3013 (w), 2939 (br), 2877 (br), 1532 (s), 1490 (m), 1463 (s), 1420 (s), 1394 (s), 1334 (m), 1273 (m), 1241 (m), 1204 (w), 1156 (s), 1098 (m), 1065 (m), 1034 (s), 1004 (w), 938 (w), 878 (w), 860 (s), 816 (s), 770 (m), 756 (s), 735 (m), 696 (w), 635 (w), 581 (w), 527 (m), 500 (w), 462 cm^{-1} (w); UV/Vis (CH_2Cl_2, $c = 2.47 \times 10^{-3}$ mol L^{-1}, 20°C): λ (ε) = 651 (186.5), 576 nm (259.5 $mol^{-1}\,dm^3\,cm^{-1}$); HRMS (EI$^+$): *m*/*z* (%): 598.0340 (9.60) $[M]^+$, 519.1220 (100.00) $[M–HBr]^+$, 437.1951 (22.98) $[M+H–2HBr]^+$, 380.2702 (16.22) [btmgp]$^+$; elemental analysis calcd (%) for $C_{22}H_{32}Br_2N_6Ni$ (599.03): C 44.11, H 5.38, N 14.03; found: C 43.48, H 5.44, N 13.18.

Crystal data for [(btmgbp)NiBr$_2$]: $C_{22}H_{32}Br_2N_6Ni$; M_r = 599.03; 0.30 × 0.25 × 0.20 mm^3; monoclinic; space group *C*2/*c*; a = 18.955(4), b = 8.8560, c = 16.665(3) Å; V = 2479.6(9) $Å^3$; Z = 4, ρ_{calcd} = 1.605 $Mg\,m^{-3}$; $Mo_{K\alpha}$ radiation (graphite monochromated, λ = 0.71073 Å); T = 200 K; θ_{range} = 2.42 to 27.55°; reflections measured 22212; independent reflections 2860; R_{int} = 0.0763; semiempirical absorption correction; final R indices [$I > 2\sigma(I)$]: $R1$ = 0.0347, $wR2$ = 0.0837.

X-ray crystallographic studies at 200 K: Suitable crystals were taken directly out of the mother liquor, immersed in perfluorinated polyether oil, and fixed on top of a glass capillary. Measurements were made using a Nonius Kappa CCD diffractometer with low-temperature unit and graphite-monochromated $Mo_{K\alpha}$ radiation. The temperature was set to 200 K. The data collected were processed using the standard Nonius software.[43] All calculations were performed using the SHELXT-PLUS software package. Structures were solved by direct methods with the SHELXS-97 program and refined with the SHELXL-97 program.[44,45] Graphical handling of the structural data during solution and refinement was performed with XPMA.[46] Structural representations were generated using Winray 32.[47] Atomic coordinates and anisotropic thermal parameters of non-hydrogen atoms were refined by full-matrix least-squares calculations.

CCDC-710399 ([(btmgb)$NiCl_2$]), -710400 ([(btmgb)$NiBr_2$]), -710401 ([(btmgn)$NiCl_2$]), -710402 ([(btmgn)$NiBr_2$]), -710403 ([(btmgp)$NiCl_2$]), -710403 ([(btmgp)$NiBr_2$]), -711925 (free btmgbp ligand), and -733600 (charge density study of [(btmgb)$NiCl_2$]) contain the supplementary crystallographic data for this paper. These data can be obtained free of charge from The Cambridge Crystallographic Data Centre via www.ccdc.cam.ac.uk/data_request/cif.

X-ray data collection and data reduction for [(btmgb)NiCl$_2$] at 7 K: Crystal data for $C_{16}H_{28}Cl_2N_6Ni$ at T = 7(1) K with graphite-monochromated $Mo_{K\alpha}$ radiation (λ = 0.71073 Å): green cuboidal crystal (0.23 × 0.30 × 0.49 mm); M_r = 434.05; monoclinic; space group $P2_1/n$ (no. 14); a = 14.0938(3), b = 10.7922(3), c = 14.3135(5) Å; β = 112.812(2)°; V = 2006.81(10) $Å^3$; Z = 4; $F(000)$ = 912; ρ_{calcd} = 1.4366(1) $g\,cm^{-3}$; μ = 1.245 mm^{-1}; 92047 Bragg reflections (3.09° < θ < 57.71°) were collected using a MAR345 IP Detector mounted on a Huber 4-circle diffractometer equipped with a 4 K Displex closed-cycle helium cryostat and a rotating anode generator (Bruker FR 591). The data was corrected for beam inhomogeneity and absorption effects using the program SORTAV (T_{min} = 0.745, T_{max} = 0.795).[48] The internal agreement factor was R_{int} (F) = 0.0248 for 20276 unique reflections.

Multipolar refinement: The deformation density was described by a multipole model[49,50] in terms of spherical harmonics multiplied by Slater-type radial functions with energy-optimized exponents [Eq. (4)]:[51]

$$\rho_{at}(\boldsymbol{r}) = P_c\rho_{core}(\boldsymbol{r}) + P_v\kappa^3\rho_{valence}(\kappa\boldsymbol{r}) + \sum_{l=0}^{l_{max}} \kappa'^3 R_l(\kappa'\boldsymbol{r}) \sum_{m=0}^{l} P_{lm\pm} d_{lm\pm}(\theta,\phi) \quad (4)$$

$\rho_{at}(\boldsymbol{r})$ is the atomic electron density, $\rho_{core}(\boldsymbol{r})$ is the core density, P_c the respective core shell population parameter, $\rho_{valence}(\kappa\boldsymbol{r})$ is the spherical valence density, P_v is the valence shell population parameter, κ is the radial screening parameter for the spherical valence density, κ' are the expansion-contraction parameters of the deformation functions, $R_l(\kappa'\boldsymbol{r})$ are normalized and nodeless radial density functions, P_{lm} are the population parameters of the respective multipoles and $d_{lm}(\theta, \phi)$ are density-normalized real spherical harmonics. In the refinement of our best model, the multipole expansion was truncated at the hexadecapole level (l_{max} = 4) for all non-hydrogen atoms. A bond-directed dipole (l_{max} = 1) was introduced for the hydrogen atoms. The atomic coordinates and displacement parameters were optimized along with all multipolar parameters using all data with $\sin\theta/\lambda < 1.00$ $Å^{-1}$. During multipolar refinements, the hydrogen positions were fixed with restrained C–H bond lengths ($r(C_{sp^2}–H)$ = 1.07 Å, $r(C_{sp^3}–H)$ = 1.09 Å) and their isotropic thermal parameters were fixed at the values obtained by the preceding independent atom-model (IAM) refinement. The final agreement factors were R_1 = 0.0271, wR = 0.0302, and GOF = 2.3449 for 13201 observed reflections ($F_o > 3\sigma(F_o)$, $\sin\theta_{max}/\lambda < 1.00$ $Å^{-1}$) and 501 parameters (N_{ref}/N_{var} = 26.4), and a featureless residual $\rho(\boldsymbol{r})$ with maximum and minimum values of 0.404 and −0.357 e $Å^{-3}$ ($\sin\theta/\lambda < 0.8$ $Å^{-1}$), respectively. Hirshfeld's rigid bond[52] test was applied to the atomic displacement parameters obtained from the refinements. The differences of mean-squares displacement amplitudes

 © 2010 Wiley-VCH Verlag GmbH & Co. KGaA, Weinheim

(DMSDA) are smaller then 0.001 Å^2 for all bonds (excluding bonds to hydrogen atoms), apart from a Ni–Cl and an Ni–N bond, which slightly exceed this value. All refinements were carried out with the full-matrix least-square program XDLSM of the XD2006 suite of programs.[53] For detailed information on data collection, data reduction, and the multipolar refinement, see sections S5–S10 of the Supporting Information.

Computational methods: The molecular geometry of the d^8 [(btmgb)$NiCl_2$] complex was optimized using the PBEPBE functional of Perdew–Burke–Ernzerhof[54] in combination with either the 6-311+G(d,p) or the TZ2P basis set as implemented in Gaussian 03[55] and ADF[56] program packages, respectively. For Cartesian coordinates of the optimized geometries, see section S14 of the Supporting Information. In the case of ADF, scalar relativistic effects were taken into account by applying the ZORA formalism.[57] If not specified otherwise, the PBEPBE/6-311+G(d,p) level of approximation will be our default method for the theoretical data specified in the text. A net charge of zero and a multiplicity of three was assumed; however, symmetry restraints were not imposed. As shown in Table 6 and section S11 of the Supporting Information, we could not identify any significant differences in the topological and geometrical parameters between the results of both computational approaches.

In the case of the ADF calculations, numerical analyses of density grid files were performed employing the INTEGRITY program by P. Rabillier et al.[58] and the program DGrid by M. Kohout[59] to analyze the topology of the electron distribution. In the case of the Gaussian 03 calculations, a local version of the AIMPAC software package[60] for the analytical evaluation of topological properties from Gaussian wavefunction files was used for this purpose. A modified version of the PROAIMV,[61] coded by C. Gatti,[62] has been used to evaluate the source function SF($\boldsymbol{r}$,Ω)[40] at the given reference points. In the case of the complementing experimental charge-density distributions, we employed the XD2006[53] package for the topological analyses. Properties of $\rho(\boldsymbol{r})$ and $\nabla^2\rho(\boldsymbol{r})$ were calculated after transformation of the local axis system into a global system.

Further quantum chemical calculations were carried out to obtain a theoretical estimate of the magnitude of the singlet–triplet energy gap (ΔE_{TS}). Here, the B3LYP[63] functional was used with a combination of two different basis sets. For the nickel atom, a Karlsruhe triple-ξ quality basis set of the second generation with a larger set of polarization functions was used (Def2-TZVPP).[64] The carbon, nitrogen, halide, and hydrogen atoms were described by a 6-311G(d,p) Pople basis set.[65] According to these hybrid DFT calculations, all complexes exhibit a triplet electronic ground state, which is in line with the experimental results. However, the choice of the bisguanidine ligand bears a strong effect on the energy difference to the first excited singlet states, ΔE_{TS} (see Table 4). Hence ΔE_{TS} is 43.3 kJ mol^{-1} for [(btmgb)$NiCl_2$] and rises to 133.1 kJ mol^{-1} for [(btmgn)$NiCl_2$. On the other hand, the influence of the halide (Cl or Br) on ΔE_{TS} is quite small except for [(btmgb)NiX_2]. Selected calculated structural parameters are contained in Table S4 of the Supporting Information.

Acknowledgements

Financial support from the Deutsche Forschungsgemeinschaft, especially through the Graduate College 850 and the priority program SPP 1178, as well as NanoCat (an International Graduate Program within the Elitenetzwerk Bayern), are all gratefully acknowledged.

[1] a) F. T. Edelmann, *Adv. Organomet. Chem.* **2008**, *57*, 183–352; b) S. Herres-Pawlis, *Nachr. Chem.* **2009**, *57*, 20–23.
[2] V. Raab, J. Kipke, R. M. Gschwind, J. Sundermeyer, *Chem. Eur. J.* **2002**, *8*, 1682–1693.
[3] S. Herres-Pawlis, A. Neuba, O. Seewald, T. Seshadri, H. Egold, U. Flörke, G. Henkel, *Eur. J. Org. Chem.* **2005**, 4879–4890.
[4] D. Petrovic, L. M. R. Hill, P. G. Jones, W. B. Tolman, M. Tamm, *Dalton Trans.* **2008**, 887–894.
[5] T. Glöge, D. Petrovic, C. Hrib, P. G. Jones, M. Tamm, *Eur. J. Inorg. Chem.* **2009**, DOI: 10.1002/ejic.200900570.
[6] L. K. Johnson, C. M. Killian, M. Brookhart, *J. Am. Chem. Soc.* **1995**, *117*, 6414–6415.
[7] See, for example: K. Wieghardt, U. Quilitzsch, B. Nuber, J. Weiss *Angew. Chem.* **1978**, *90, 381–382; Angew. Chem. Int. Ed. Engl.* **1978**, 17, 351–352; *Angew. Chem. Int. Ed. Engl.* **1978**, *17*, 351–352.
[8] a) D. Herebian, K. Wieghardt, F. Neese, *J. Am. Chem. Soc.* **2003**, *125*, 10997–11005; b) K. Ray, T. Petrenko, K. Wieghardt, F. Neese, *Dalton Trans.* **2007**, 1552–1566.
[9] O. Siri, P. Braunstein, M.-M. Rohmer, M. Bénard, R. Welter, *J. Am. Chem. Soc.* **2003**, *125*, 13793–13803.
[10] A. Peters, E. Kaifer, H.-J. Himmel, *Eur. J. Org. Chem.* **2008**, 5907–5914.
[11] See, for example: a) C. K. Jorgenson, *Coord. Chem. Rev.* **1966**, *1*, 164–178; b) J. S. Miller, K. S. Min, *Angew. Chem.* **2009**, *121*, 268–278; *Angew. Chem. Int. Ed.* **2009**, *48*, 262–272.
[12] Recently we synthesized the first complex of the radical monocation [btmgb]$^{+\bullet}$: A. Peters, C. Trumm, M. Reinmuth, D. Emeljanenko, E. Kaifer, H.-J. Himmel, unpublished results.
[13] A. L. Balch, R. H. Holm, *J. Am. Chem. Soc.* **1966**, *88*, 5201–5209.
[14] See also the discussion in: P. Chaudhuri, C. N. Verani, E. Bill, E. Bothe, T. Weyhermüller, K. Wieghardt, *J. Am. Chem. Soc.* **2001**, *123*, 2213–2223.
[15] S.-M. Peng, C.-T. Chen, D.-S. Liaw, C.-I. Chen, Y. Wang, *Inorg. Chim. Acta* **1985**, *101*, L31–L33.
[16] M. M. Khusniyarov, K. Harms, O. Burghaus, J. Sundermeyer, B. Sarkar, W. Kaim, J. van Slageren, C. Duboc, J. Fiedler, *Dalton Trans.* **2008**, 1355–1365.
[17] D. Venegas-Yazigi, H. Mirza, A. B. P. Lever, A. J. Lough, J. Costamagna, R. Latorre, *Acta Crystallogr. Sect. C* **2000**, *56*, e281–e282.
[18] M. Kawahata, K. Yamaguchi, T. Ito, T. Ishikawa, *Acta Crystallogr. Sect. E* **2006**, *62*, o3301–o3302.
[19] P. Pruszynski, K. T. Leffek, B. Borecka, T. S. Cameron, *Acta Crystallogr. Sect. C* **1992**, *48*, 1638–1641.
[20] A. Peters, U. Wild, O. Hübner, E. Kaifer, H.-J. Himmel, *Chem. Eur. J.* **2008**, *14*, 7813–7821.
[21] U. Wild, O. Hübner, A. Maronna, M. Enders, E. Kaifer, H. Wadepohl, H.-J. Himmel, *Eur. J. Inorg. Chem.* **2008**, 4440–4447.
[22] J.-O. Dalbavie, J.-B. Regnouf-de-Vains, R. Lamartine, M. Perrin, S. Lecocq, B. Fenet, *Eur. J. Inorg. Chem.* **2002**, 901–909.
[23] D. J. Darensbourg, K. K. Klausmeyer, J. H. Reibernspies, *Inorg. Chem.* **1996**, *35*, 1535–1539.
[24] T. Yamasaki, N. Ozaki, Y. Saika, K. Ohta, K. Goboh, F. Nakamura, M. Hashimoto, S. Okeya, *Chem. Lett.* **2004**, *33*, 928–929.
[25] R. W. Alder, P. S. Bowman, W. R. S. Steele, D. R. Winterman, *J. Chem. Soc. Chem. Commun.* **1968**, 723–724.
[26] S. N. Gamage, R. H. Morris, S. J. Rettig, D. C. Thackray, I. S. Thorburn, B. R. James, *J. Chem. Soc. Chem. Commun.* **1987**, 894–895.
[27] G. N. La Mar, W. DeW. Horrocks, Jr., R. H. Holm, *NMR of Paramagnetic Molecules—Principles and Applications*, Academic Press, New York, **1973**.
[28] This contribution has been roughly estimated using the expression $\chi_{dia} = -0.79 \times Z_i \times 10^{-6}$ $(r/a_0)^2$ emu mol^{-1}, in which Z_i is the sum of all core electrons per formula unit and $(r/a_0)^2 = 1$ (a_0 is the Bohr radius, r the mean ionic radius).
[29] a) O. Kahn, *Molecular Magnetism*, VCH, Weinheim, **1993**. Resulting from the value of μ_{eff}, the compound possesses a total angular moment with $J = 1$. In this instance, two unpaired electrons are present and the orbital moment L is assumed to be quenched; b) *Compendium of Chemical Terminology*, Blackwell, New York, **1996**, p. 2284.
[30] R. Boa, *Coord. Chem. Rev.* **2004**, *248*, 757–815.
[31] H. Frydendahl, H. Toftlund, J. Becher, J. C. Dutton, K. S. Murray, L. F. Taylor, O. P. Anderson, E. R. T. Tiekink, *Inorg. Chem.* **1995**, *34*, 4467–4476.

 © 2010 Wiley-VCH Verlag GmbH & Co. KGaA, Weinheim

[32] H. R. Jiménez, J. Salgado, J. M. Moratal, I. Morgenstern-Badarau, *Inorg. Chem.* **1996**, *35*, 2737–2741.

[33] See, for example a) G. Eickerling, R. Mastalerz, V. Herz, W. Scherer, H.-J. Himmel, M. Reiher, *J. Chem. Theory Comput.* **2007**, *3*, 2182–2197; b) B. Rohrmoser, G. Eickerling, M. Presnitz, W. Scherer, V. Eyert, R.-D. Hoffmann, U. C. Rodewald, C. Vogt, R. Pöttgen, *J. Am. Chem. Soc.* **2007**, *129*, 9356–9365; c) D. Himmel, N. Trapp, I. Krossing, S. Altmannshofer, V. Herz, G. Eickerling, W. Scherer, *Angew. Chem.* **2007**, *119*, 8445–8449; *Angew. Chem. Int. Ed.* **2007**, *46*, 8295–8300.

[34] Cl-Ni-Cl valence angles of about 130° have been also found for d^8 $[LNiCl_2]$ complexes in which L represents a chelating diamine or a 2,2′-bipyridyl (bipy) ligand: for example, ∢Cl-Ni-Cl = 127.25(4)° in $[(itmeda)NiCl_2]$ (itmeda = *N*-isopropyl-*N*,*N*′,*N*′-trimethylethane-1,2-diamine); ∢Cl-Ni-Cl = 129.26(7)° in $[(tmpn)NiCl_2]$ (tmpn = tetramethylpropane-1,2-diamine); ∢Cl-Ni-Cl = 126.50(2)° in $[(teeda)NiCl_2]$ (teeda = *N*,*N*,*N*′,*N*′-tetraethylenediamine); ∢Cl-Ni-Cl = 132.93(3)° in $[(6,6'\text{-}Me_2bipy)NiCl_2]$; a) A. Johansson, E. Wingstrand, M. Håkansson, *Inorg. Chim. Acta* **2005**, *358*, 3293–3302; b) D. A. Handley, P. B. Hitchcock, G. F. Leigh, *Inorg. Chim. Acta* **2001**, *314*, 1–13; c) W. J. Marshall, V. V. Grushin, *Can. J. Chem.* **2005**, *83*, 640–645. Unfortunately, no magnetic susceptibility studies were reported for these complexes.

[35] a) S. Zein, F. Neese, *J. Phys. Chem. A* **2008**, *112*, 7976–7983; b) S. Zein, C. Duboc, W. Lubitz, F. Neese, *Inorg. Chem.* **2008**, *47*, 134–142.

[36] a) C. Duboc, T. Phoeung, S. Zein, J. Pécaut, M. N. Collomb, F. Neese, *Inorg. Chem.* **2007**, *46*, 4905–4916; b) F. Neese, *J. Am. Chem. Soc.* **2006**, *128*, 10213–10222.

[37] The π character of a bond may be revealed by the bond ellipticity, ε, which measures the asymmetry of the charge distribution between two bonded atoms at the bond critical point; a) R. F. W. Bader, T. S. Slee, D. Cremer, E. Kraka, *J. Am. Chem. Soc.* **1983**, *105*, 5061–5068; b) D. Cremer, E. Kraka, T. S. Slee, R. F. W. Bader, C. D. H. Lau, T. T. Nguyen-Dang, P. J. MacDougall, *J. Am. Chem. Soc.* **1983**, *105*, 5069–5075.

[38] a) W. Scherer, P. Sirsch, D. Shorokhov, G. S. McGrady, S. Mason, M. G. Gardiner, *Chem. Eur. J.* **2002**, *8*, 2324–2334; b) J. R. Cheeseman, M. T. Carroll, R. F. W. Bader, *Chem. Phys. Lett.* **1988**, *143*, 450–458; c) M. Tafipolsky, W. Scherer, K. Öfele, G. Artus, B. Pedersen, W. A. Herrmann, G. S. McGrady, *J. Am. Chem. Soc.* **2002**, *124*, 5865–5880; d) W. Scherer, P. Sirsch, D. Shorokhov, M. Tafipolsky, G. S. McGrady, E. Gullo, *Chem. Eur. J.* **2003**, *9*, 6057–6070; e) W. Scherer, G. S. McGrady, *Angew. Chem.* **2004**, *116*, 1816–1842; *Angew. Chem. Int. Ed.* **2004**, *43*, 1782–1806.

[39] R. F. W. Bader and co-workers have demonstrated that the negative Laplacian of the charge-density distribution, $L(\boldsymbol{r}) = -\nabla^2\rho\boldsymbol{r}$, determines where the charge-density distribution is locally concentrated ($L(\boldsymbol{r}) > 0$) or locally depleted ($L(\boldsymbol{r}) < 0$). Accordingly, the $L(\boldsymbol{r})$ function can be employed to resolve the shell structure for elements with $Z > 18$. However, the shell structure of the transargonic elements is not fully represented by the Laplacian. In general the fourth, fifth, or sixth shell for elements of Periods 4–6, respectively, is not revealed in the Laplacian. As a convention, Bader and coworkers suggested that the outermost shell of charge concentration (CC) of an atom (second shell of CC of the carbon atoms and third shell of CC of the nickel atom) represents its (effective) valence shell charge concentration (VSCC); a) R. F. W. Bader, P. J. MacDougall, C. D. H. Lau, *J. Am. Chem. Soc.* **1984**, *106*, 1594–1605; b) R. F. W. Bader, H. Essén, *J. Chem. Phys.* **1984**, *80*, 1943–1960; c) R. P. Sagar, A. C. T. Ku, V. Smith, *J. Chem. Phys.* **1988**, *88*, 4367–4374; d) Z. Shi, R. J. Boyd, *J. Chem. Phys.* **1988**, *88*, 4375–4377; e) W.-T. Chan, I. P. Hamilton, *J. Chem. Phys.* **1998**, *108*, 2473–2485; f) M. Kohout, A. Savin, H. Preuss, *J. Chem. Phys.* **1991**, *95*, 1928–1933; g) R. F. W. Bader, R. J. Gillespie, F. Martín, *Chem. Phys. Lett.* **1998**, *290*, 488–494; h) G. S. McGrady, A. Haaland, H. P. Verne, H. V. Volden, A. J. Downs, D. Shorokhov, G. Eickerling, W. Scherer, *Chem. Eur. J.* **2005**, *11*, 4921–4934; i) G. Eickerling, M. Reiher, *J. Chem. Theory Comput.* **2008**, *4*, 286–296.

[40] a) R. F. Bader, C. Gatti, *Chem. Phys. Lett.* **1998**, *287*, 233–238; b) C. Gatti, D. Lasi, *Faraday Discuss.* **2007**, *135*, 55–78. For more recent applications, see, for example: c) J. Overgaard, H. F. Clausen, J. A. Platts, B. B. Iversen, *J. Am. Chem. Soc.* **2008**, *130*, 3834–3843; d) G. S. McGrady, P. Sirsch, N. P. Chatterton, A. Ostermann, C. Gatti, S. Altmannshofer, V. Herz, G. Eickerling, W. Scherer, *Inorg. Chem.* **2009**, *48*, 1588–1598; e) L. J. Farrugia, C. Evans, D. Lentz, M. Roemer, *J. Am. Chem. Soc.* **2009**, *131*, 1251–1268; f) L. Lo Presti, C. Gatti, *Chem. Phys. Lett.* **2009**, *476*, 308–316; g) L. J. Farrugia, P. Macchi, *J. Phys. Chem. A* **2009**, *113*, 10058–10067.

[41] W. Scherer, G. Eickerling, D. Shorokhov, E. Gullo, G. S. McGrady, P. Sirsch, *New J. Chem.* **2006**, *30*, 309–312.

[42] M. Kawahata, K. Yamaguchi, T. Ito, T. Ishikawa, *Acta Crystallogr. Sect. E* **2006**, *62*, o3301–o3302.

[43] Nonius, DENZO-SMN, Data processing software, **1998**, http://www.nonius.com.

[44] a) SHELXS-97, Program for Crystal Structure Solution, G. M. Sheldrick, University of Göttingen, Göttingen **1997**, http://shelx.uni-ac.gwdg.de/SHELX/index.html; b) SHELXL-97, Program for Crystal Structure Refinement, G. M. Sheldrick, University of Göttingen, Göttingen, **1997**, http://shelx.uni-ac.gwdg.de/SHELX/index.html.

[45] *International Tables for X-ray Crystallography, Vol. 4*, Kynoch Press, Birmingham, **1974**.

[46] XPMA, L. Zsolnai, G. Huttner, University of Heidelberg, Heidelberg, **1994**, http://www.uni-heidelberg.de/institute/fak12/AC/huttner/software/software.html.

[47] Winray 32, R. Soltek, University of Heidelberg, Heidelberg, **2000**; http://www.uni-heidelberg.de/institute/fak12/AC/huttner/software/software.html.

[48] R. H. Blessing, *Acta Crystallogr. Sect. A* **1995**, *51*, 33.

[49] R. F. Stewart, *Acta Crystallogr. Sect. A* **1976**, *32*, 565–574.

[50] H. K. Hansen, P. Coppens, *Acta Crystallogr. Sect. A* **1978**, *34*, 909–921.

[51] P. Macchi, A. Volkov, unpublished results.

[52] F. L. Hirshfeld, *Acta Crystallogr. Sect. A* **1976**, *32*, 239–244.

[53] XD2006 (version 5.42): A. Volkov, P. Macchi, L. J. Farrugia, C. Gatti, P. Mallinson, T. Richter, T. Koritsanszky, A computer program for multipole refinement, topological analysis of charge densities, and evaluation of intermolecular energies from experimental or theoretical structure factors, **2006**.

[54] a) J. P. Perdew, K. Burke, M. Ernzerhof, *Phys. Rev. Lett.* **1996**, *77*, 3865–3868; b) J. P. Perdew, K. Burke, M. Ernzerhof, *Phys. Rev. Lett. Am. Phys. Soc* **1997**, *78*, 1396–1396.

[55] Gaussian 03, Revision B.03, M. J. Frisch, G. W. Trucks, H. B. Schlegel,G. E. Scuseria, M. A. Robb, J. R. Cheeseman, J. A. Montgomery, Jr., T. Vreven, K. N. Kudin, J. C. Burant, J. M. Millam, S. S. Iyengar, J.Tomasi, V. Barone, B. Mennucci, M. Cossi, G. Scalmani, N. Rega, G. A. Petersson, H. Nakatsuji, M. Hada, M. Ehara, K. Toyota, R. Fukuda, J. Hasegawa, M. Ishida, T. Nakajima, Y. Honda, O. Kitao, H. Nakai, M. Klene, X. Li, J. E. Knox, H. P. Hratchian, J. B. Cross, V. Bakken, C. Adamo, J. Jaramillo, R. Gomperts, R. E. Stratmann, O. Yazyev, A. J. Austin, R. Cammi, C. Pomelli, J. W. Ochterski, P. Y. Ayala, K. Morokuma, G. A. Voth, P. Salvador, J. J. Dannenberg, V. G. Zakrzewski, S. Dapprich, A. D. Daniels, M. C. Strain, O. Farkas, D. K.Malick, A. D. Rabuck, K. Raghavachari, J. B. Foresman, J. V. Ortiz, Q. Cui, A. G. Baboul, S. Clifford, J. Cioslowski, B. B. Stefanov, G. Liu, A. Liashenko, P. Piskorz, I. Komaromi, R. L. Martin, D. J. Fox, T. Keith, M. A. Al-Laham, C. Y. Peng, A. Nanayakkara, M. Challacombe, P. M. W. Gill, B. Johnson, W. Chen, M. W. Wong, C. Gonzalez, J. A. Pople, Gaussian Inc., Wallingford CT, **2004**.

[56] ADF2007.01, SCM, Theoretical Chemistry, Vrije Universiteit Amsterdam, http://www.scm.com.

[57] a) E. van Lenthe, J. Snijders, E. Baerends, *J. Chem. Phys.* **1996**, *105*, 6505–6516; b) E. van Lenthe, J. Snijders, E. Baerends, *J. Chem. Phys.* **1999**, *110*, 8943–8953.

[58] C. Katan, P. Rabillier, C. Lecomte, M. Guezo, V. Oison, M. Souhassou, *J. Appl. Crystallogr.* **2003**, *36*, 65–73.

 © 2010 Wiley-VCH Verlag GmbH & Co. KGaA, Weinheim

[59] Program DGrid 4.2, M. Kohout, Max Planck Institute for Chemical Physics of Solids, Dresden, **2008**.
[60] a) F. W. Biegler-König, R. F. W. Bader, T. Tang, *J. Comput. Chem.* **1982**, *3*, 317–328; b) J. R. Cheeseman, T. A. Keith, R. F. W. Bader, AIMPAC program package, McMaster University, Ontario, **1997**.
[61] PROAIMV, Version 94, Revision B, part of the AIMPAC program package. See reference [60].
[62] a) C. Gatti, L. Bertini, *Acta Crystallogr. Sect. A* **2004**, *60*, 438–449; b) C. Gatti, SF ESI codes, private communication.
[63] a) A. D. Becke, *J. Chem. Phys.* **1993**, *98*, 5648–5652; b) C. Lee, W. Yang, R. G. Parr, *Phys. Rev. B* **1988**, *37*, 785–789.
[64] F. Weigend, R. Ahlrichs, *Phys. Chem. Chem. Phys.* **2005**, *7*, 3297–3305.
[65] R. Krishnan, J. S. Binkley, R. Seeger, J. A. Pople, *J. Chem. Phys.* **1980**, *72*, 650–654.

Received: June 2, 2009
Revised: October 8, 2009
Published online: December 4, 2009

 © 2010 Wiley-VCH Verlag GmbH & Co. KGaA, Weinheim